Setup of a Laser for Cooling of Calcium Monofluoride Molecules

Bachelor's Thesis by
Alexandra Liliane Köpf

5th Institute of Physics
University of Stuttgart

February 24, 2023

Examiner: Prof. Dr. Tilman Pfau

University of Stuttgart
5th Institute of Physics

Declaration of Authorship

I hereby certify that this thesis is entirely my own work except where otherwise indicated. Passages and ideas from other sources have been clearly indicated. Neither this nor a similar work has been presented to an examination committee. The electronic and printed versions of this thesis are identical.

Stuttgart, February 24, 2023 Alexandra Liliane Köpf

Abstract

The complex energy level structure of diatomic molecules requires a larger number of lasers to perform laser cooling than in the case of atoms. In this thesis, a laser system operating on the $X^2\Sigma^+(v = 2) \rightarrow A^2\Pi_{1/2}(v = 1)$ transition of calcium monofluoride (CaF) is set up and characterized. The laser is the second repump laser with a wavelength of 628.1 nm and constructed as an external cavity diode laser. Since this transition requires multiple frequency sidebands to address the hyperfine splitting of the groundstate in CaF, the laser light is modulated with an electro-optical phase modulator. Moreover, this second repump laser as well as the already set up first repump laser are frequency locked with a scanning transfer cavity.

Zusammenfassung

Aufgrund der komplexen Energieniveaus von zweiatomigen Molekülen wird eine größere Anzahl von Lasern für Laserkühlung benötigt als im Fall von Atomen. Im Rahmen dieser Bachelorarbeit wird ein Lasersystem für den $X^2\Sigma^+(v = 2) \rightarrow A^2\Pi_{1/2}(v = 1)$ Übergang von Calciumfluorid (CaF) aufgebaut und charakterisiert. Der Laser ist der zweite Rückpumplaser mit einer Wellenlänge von 628.1 nm und ist als Diodenlaser mit externem Resonator konstruiert. Da dieser Übergang Seitenbänder im Frequenzspektrum des Lasers erfordert, um die Hyperfeinaufspaltung des Grundzustands in CaF zu erreichen, wird das Laserlicht mit einem elektro-optischen Phasenmodulator moduliert. Zudem wird die Frequenz dieses zweiten sowie des bereits aufgebauten ersten Rückpumplasers mithilfe eines Transferresonators stabilisiert.

Contents

1 Introduction

The concept of cooling atoms by using laser light to exert a force on them was first proposed in the 1970s [1]. The motivation for early developments in laser cooling was to improve the accuracy of spectroscopic measurements and atomic clocks [2]. Since the first cooling of magnesium ions [3] and neutral sodium atoms [4] laser cooling technology has become an important basis for a rapidly developing field of science. For example magneto-optical traps, which utilize laser cooling, are integral for quantum computing and quantum simulation with neutral atoms. The low temperatures made available due to laser cooling also enable more accurate precision measurements, such as investigations into the time variation of fundamental constants [5].
Ultracold molecules provide a more complex system than atoms and are therefore interesting for many different applications. The application of laser cooling to molecules increases the complexity of the systems that can be simulated in a quantum simulator. Molecules with large electric dipole moments can interact strongly with each other due to long-range dipole-dipole interactions. For example spin lattice models can be simulated by interacting polar molecules in an optical lattice [6]. Measurements with molecules at ultracold temperatures provide new possibilities for precision measurements and can be used to test fundamental physics. The electric dipole moment of an electron for example has been measured with high precision by using cold polar molecules [7]. Additionally, physics beyond the Standard Model of particle physics, which states the fundamental constants to be fixed parameters, can be investigated by testing theories about dark energy, which propose that the fundamental constants change with time or position [8, 9]. Experiments with ultracold molecules can also provide new insights to the basic building blocks of chemical reactions [10, 11].
However, molecules made up of multiple atoms have rotational and vibrational degrees of freedom. Therefore, their energy level structure is significantly more complex than that of atoms. This makes it very difficult to find a molecular species with a closed cycling transition required for effective slowing and cooling [2]. A group of promising molecular species with favorable cycling properties has been identified in the 2000s [12]. These alkaline-earth monohydride radicals include one electron, whose electronic excitation only changes the internuclear bond in a negligible way, leading to a promising cycling behavior.
In the last ten years, there have been great improvements in the achievable phase space density of molecular quantum gases, that have increased by ten orders of magnitude over the last ten years [13]. This has brought the goal of a degenerate quantum gas of laser cooled molecules within reach. Motivated by these developments, a new experiment has been developed in the Cold Molecules group at the

5th Institute of Physics of the University of Stuttgart with the goal of creating a Bose-Einstein condensate of calcium monofluoride molecules. Based on the development of dipolar quantum gases with dysprosium, this experiment is intended to probe further into the phase space diagram of supersolid quantum gases. This is a new state of matter which is characterized by the frictionless fluid flow of superfluids as well as the crystalline structure of solids. This advance is made possible by the large electric dipole moment of calcium monofluoride and the fact that the dipolar length of molecules can be tuned in contrast to dysprosium atoms. Therefore, different phases in the phase diagram can be observed [14].
CaF molecules are suitable for laser cooling due to their energy level structure, which features highly diagonal Franck-Condon factors. As a CaF molecule is unlikely to change its vibrational state during an electronic transition, this enables closed cycling of the $X^2\Sigma^+(N=1) \rightarrow A^2\Pi_{1/2}(J=1/2, p=+)$ transition with only two significant loss channels into higher vibrational states. These are addressed by two repump lasers to bring the molecules back into the cooling cycle and allow for effective laser cooling [2].
The aim of this thesis is the construction and characterization of an external cavity diode laser to drive the second repump transition with a wavelength of $\lambda = 628.1\,\mathrm{nm}$. Moreover, the second repump laser is locked on a transfer cavity and modulated with an electro-optical modulator to create the frequency sidebands required to address the hyperfine splitting of the ground state in CaF.

2 Theoretical Background

2.1 Laser Cooling

Laser cooling is a cooling technique for atoms or molecules that makes use of the fact that the interaction with light can also change an atom's momentum. This section provides an overview of the basic concepts of laser cooling for a simple two-level atom and the more complicated case of molecules.

2.1.1 Laser Cooling of Atoms

The atoms are assumed to have two internal states connected by a transition with angular frequency ω_0. This is illustrated in figure 1.

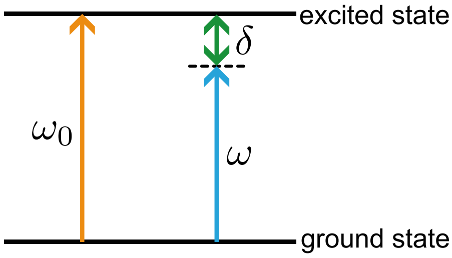

Figure 1: Energy levels of a two-level atom with transition frequency ω_0 and red-detuned laser frequency ω.

Atoms interacting with the light of a laser that is on resonance with the atomic transition can absorb a photon from the beam. Since the total momentum is conserved in this process, the atom gets an additional momentum of $\hbar\vec{k}$, where $\hbar$ is the reduced Planck constant and $\vec{k}$ the wave vector of the photon.
However, in an atom cloud at room temperature, atoms or molecules are moving with a typical speed of 300 m/s in random directions and the laser frequency gets shifted by the Doppler effect [2]. Due to the finite lifetime of the excited state, the atom then reemits a photon and decays to the ground state again. The emission process also causes a momentum transfer to the atom. But since the photon is emitted in a random direction, this effect can be neglected, as the momentum contribution of the emission process averages to zero after many scattering cycles. Therefore, the total force acting on the atom is pointing in the direction of the laser beam.
For laser cooling, two identical counter-propagating laser beams can interact with the atoms, as shown in figure 2(a). The laser frequency ω is not on resonance with

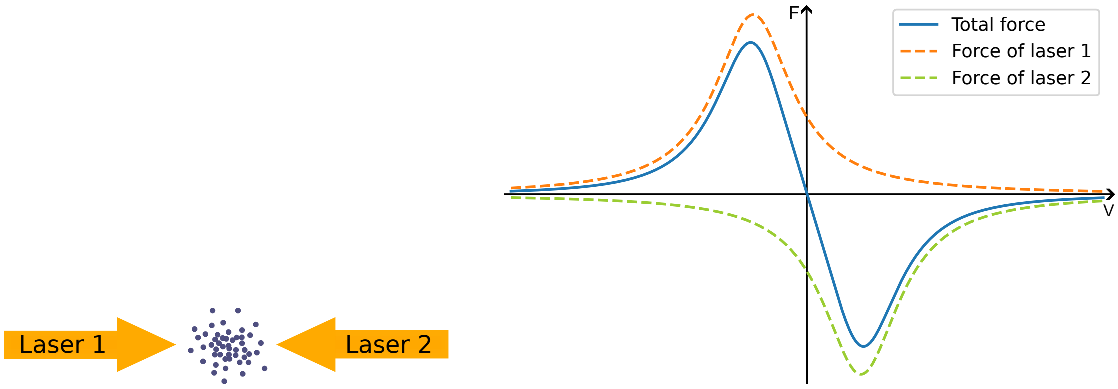

(a) (b)

Figure 2: (a) Two identical counter-propagating laser beams interacting with a cloud of atoms for laser cooling. (b) Force on an atom for laser cooling with two counter-propagating red-detuned laser beams. The total force is the sum of the forces resulting from both individual lasers.

atomic transition but slightly smaller and therefore called "red-detuned". The detuning is defined as the frequency difference $\delta = \omega - \omega_0$. For atoms moving in the same direction as the laser beam, the effective frequency of the laser decreases, whereas it increases for atoms counter-propagating the laser beam. Therefore, the detuning becomes $\delta_{\mathrm{D}} = \delta - kv$ for an atom moving with a velocity v. The detuning can be compensated by the Doppler shift since atoms moving in the opposite direction as a laser beam become resonant with this laser and are more likely to absorb a photon of it. Thus, the atoms are slowed down by most likely absorbing photons moving in the opposite direction. For an atom cloud in three dimensions, three pairs of lasers in all spatial directions are needed to reduce the velocity components in all directions.
The resulting total force in one dimension as a function of the velocity of an atom is depicted in figure 2(b) and shows that in the case of red detuning the total force acting on moving atoms is directed in the opposite direction of their velocity. The total force is the sum of the forces resulting from both individual lasers. During one scattering event an atom's velocity is changed by the recoil velocity $v_{\mathrm{r}} = \hbar k/m$ where m is the atom mass. This velocity is of the order of $v_{\mathrm{r}} \sim 0.03\,\mathrm{m/s}$. Thus, approximately 10^4 scattering events are required to cool atoms efficiently [2]. However, energy levels in real atoms are more complicated than a simple two-level system. It is therefore important that an atom that has been excited does not decay into a state where it is no longer resonant with the applied laser light. To have such a closed cycle is necessary so that the atoms do not leave the cooling cycle after too few scattering events.

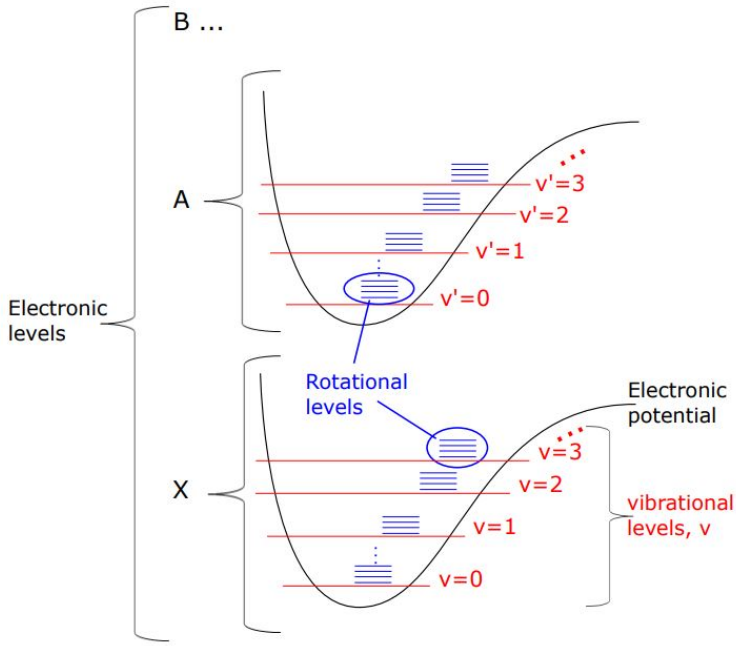

Figure 3: Schematic energy level structure of a diatomic molecule with electronic, vibrational and rotational levels. Figure taken from [17].

2.1.2 Energy Level Structure of Molecules

As molecules are made up of multiple atoms, they have more internal degrees of freedom than atoms. This makes the energy level structure more complicated than in atoms. Therefore, it can be challenging to find a closed transition. Figure 3 shows the schematic energy level structure of a diatomic molecule. Only the case of diatomic molecules is discussed here. For polyatomic molecules such as SrOH [15] or CaOH [16] there are further degrees of freedom that complicate the laser cooling schemes significantly.

Diatomic molecules have different electronic energy levels that are labeled X for the ground state and alphabetically A, B, C, ... for all higher levels [17]. The nuclei of a molecule have a potential energy that is a function of their distance R and describes a repulsion of both nuclei at low distances and attraction at large distances as shown in figure 3.

The electronic energy also acts as a potential for oscillations of the atoms in the molecule around an equilibrium distance R_e. As a result there is a set of vibrational energy levels on top of each electronic level. By solving the Schrödinger equation for the corresponding potential curve $E_\mathrm{el}(R)$, one can derive the wave functions $\Phi_{\mathrm{el,v}}(R)$ and the quantized energy levels E_vib described by the quantum

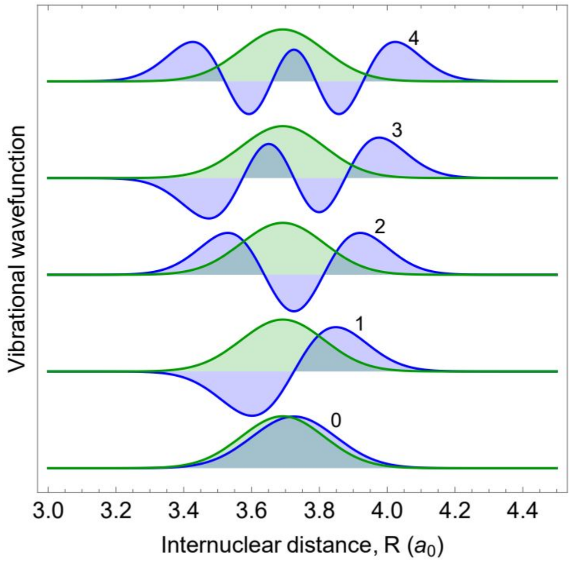

Figure 4: Vibrational wave functions $\Phi_{\mathrm{v'=0}}$ of the first excited state (green) and Φ_{v} of the ground state for $v = 0, 1, 2, 3, 4$ (blue). Figure taken from [2].

number $v = 0, 1, 2, ...$ For small oscillations around R_e one can approximate the potential to be harmonic. The solutions are therefore those of the quantum mechanical harmonic oscillator with $E_{\mathrm{vib}} \approx (v + 1/2)\hbar\omega_e$ and the harmonic oscillator frequency ω_e [18].
In addition to the vibrational degrees of freedom, molecules also have rotational degrees of freedom. Thus, there is a set of rotational energy levels for each vibrational state. In the simplified model of the molecule as a rigid rotor, these energy levels are $E_{\mathrm{rot}} = \frac{\hbar^2}{2I} \cdot N(N+1)$, where I is the moment of inertia and $N = 0, 1, 2, ...$ is the quantum number labeling the quantized levels [18].
The gap between two adjacent electronic levels is usually of the order of several 100 THz while the gap between vibrational levels of the same electronic state is of the order of 10 THz. The gap between adjacent rotational levels is only of the order of 20 GHz [18].
When a molecule in the excited state $A(v')$ decays back into the ground state X there is no selection rule into which vibrational level of X it can decay. Instead the probability for the transition between $A(v')$ and $X(v)$ is given by the Franck-Condon factor

$$P(v', v) = \left| \int \Phi_{\mathrm{A,v'}}(R)\Phi_{\mathrm{X,v}}(R)dR \right|^2, \tag{2.1}$$

which describes the overlap of the two corresponding vibrational wave functions.
If the internuclear distance of two different electronic states is similar, both states

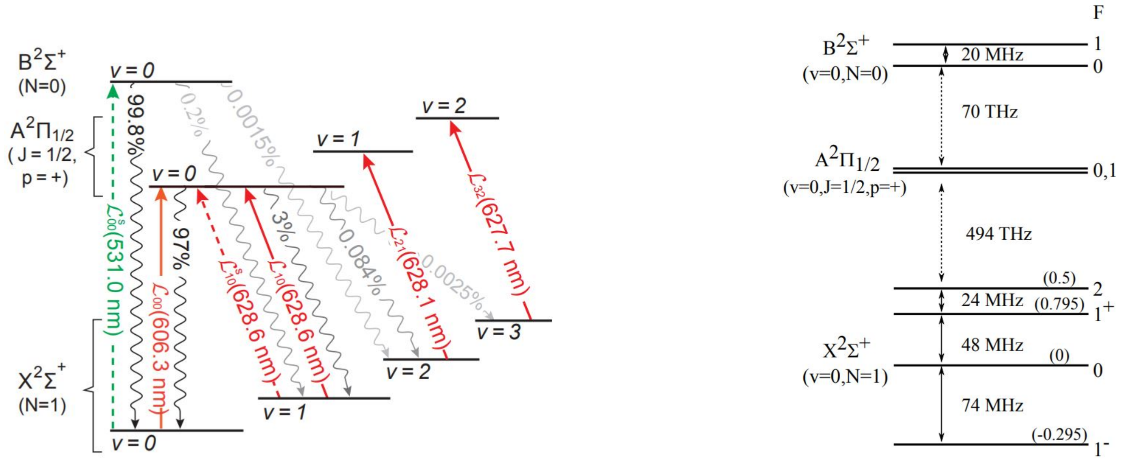

(a) (b)

Figure 5: Level schemes for CaF molecules. (a) Relevant energy levels with their vibrational splitting and the respective decay probabilities (gray lines). The slowing transition and corresponding repump transition are indicated by dotted lines, the cooling transition with three repump lasers by solid lines. Figure taken from [19]. (b) Hyperfine splitting of the vibrational ground states of X, A and B. Figure taken from [17].

have similar potential curves. Thus, the vibrational wave functions with same v in the ground and excited state are nearly identical to each other. A molecule in the excited state $A(v' = 0)$ is then most likely to decay back into the state $X(v = 0)$ due to the high overlap of both vibrational wave functions. The probability to decay into a ground state with $v > 0$ is decreasing with increasing v as the wave function overlap is very small [18].

2.1.3 Energy Levels of CaF

Since about 10^4 photons need to be scattered in order to cool molecules from room temperature, losses into different vibrational levels have to be avoided. Therefore, all transitions with a decay probability higher than 10^{-4} need to be addressed with a repump laser that brings the molecules back into the cooling cycle [2]. However, this is only practical for molecules with highly diagonal Franck-Condon factors that only require a small number of repump lasers.
Calcium monofluoride (CaF) satisfies this requirement. The calcium atom in CaF provides two valence electrons. Only one is responsible for the ionic bond to the fluorine atom while the other electron can be excited into a higher electronic state.

The distance R_{e} barely changes during the transition [2]. Figure 4 shows the wave function $\Phi_{\mathrm{v'=0}}$ of the A state in green as well as Φ_{v} for $v = 0, 1, 2, 3$ and 4 of the X state in blue. The resulting decay probabilities are shown in figure 5(a). Only one laser for the main cooling transition and two repump lasers are required since all probabilities to decay into states with $v \geq 3$ are small enough to be neglected.
Figure 5(a) shows the energy levels of CaF molecules that are relevant for slowing and cooling the molecules. The transition used for slowing the CaF beam is $X^2\Sigma^+(v = 0) \rightarrow B^2\Sigma^+(v = 0)$, which has a wavelength of $\lambda = 531.0\,\mathrm{nm}$ and also has highly diagonal Franck-Condon factors. The $X^2\Sigma^+(v = 1) \rightarrow A^2\Pi_{1/2}(v = 0)$ transition is used for repumping, in order to address the most relevant loss channel. The slowing transition is sufficiently closed with only one repump laser [17].
The transition $X^2\Sigma^+(v = 0) \rightarrow A^2\Pi_{1/2}(v = 0)$ is used for cooling the molecules. The transitions $X^2\Sigma^+(v = 1) \rightarrow A^2\Pi_{1/2}(v = 0)$ and $X^2\Sigma^+(v = 2) \rightarrow A^2\Pi_{1/2}(v = 1)$ are addressed by repump lasers with corresponding wavelengths of $\lambda = 628.6\,\mathrm{nm}$ and $\lambda = 628.1\,\mathrm{nm}$. A possible third repump laser could drive the transition $X^2\Sigma^+(v = 3) \rightarrow A^2\Pi_{1/2}(v = 2)$ with $\lambda = 627.7\,\mathrm{nm}$.
The transitions for the second and third repump laser are chosen to bring the molecules into the states $A(v = 1)$ and $A(v = 2)$ instead of directly to the $A(v = 0)$ state. This is due to the effective scattering rate of the transitions

$$\Gamma_{\mathrm{eff}} \propto \frac{N_{\mathrm{e}}}{N_{\mathrm{g}} + N_{\mathrm{e}}} \cdot \Gamma \tag{2.2}$$

where N_{e} and N_{g} are the numbers of excited and ground states. Repumping to the states $A(v = 1)$ and $A(v = 2)$ increases the number of excited states involved in the cycle, which in turn increases the scattering rate. This is advantageous since the scattering rate directly affects the achievable magnitude of the scattering force [20].
The different energy levels also show a hyperfine splitting since the fluorine atom has a nuclear spin of $I = 1/2$. This substructure is depicted in figure 5(b) for the vibrational ground states of the levels X, A and B with $v = 0$. For higher vibrational quantum numbers, the splitting is very similar. While the hyperfine states of the A state cannot be resolved with the cooling laser, the four sublevels of the ground state X have to be adressed separately [17]. This can be done by using a single laser and creating frequency sidebands with electro-optic modulation [21].

2.2 Diode Lasers

Diode lasers are routinely used for experiments with cold atoms or molecules to produce the light required to manipulate these particles. Diode lasers have the advantage that they are flexible in their wavelength and also relatively easy to set up. The following section gives an overview of laser theory and its application to diode lasers.

2.2.1 Working Principle of Lasers

A laser is a light source that produces coherent electromagnetic waves with a very narrow frequency spectrum. Therefore, they can be used to drive the transitions for laser cooling or slowing.
Lasers consist of an active medium in which a population inversion is achieved so that higher energy states are populated more than lower ones. Since this population deviates from thermal equilibrium, the medium has to be pumped by an external energy source to excite the atoms to a higher state. A population inversion is not possible for a two-level system. Photons, emitted due to spontaneous decay of the excited state in the active medium, can cause further photons to be emitted by stimulated emission. The light gets further amplified by a resonator outside the active medium. Photons are reflected back and forth in the active medium and cause stimulated emission, which produces an avalanche of identical photons [22].

2.2.2 Laser Diodes

In a laser diode, the active medium is given by a junction of two semiconductor materials. One of them is n-doped, which means that a current can be conducted by additional valence electrons of impurities in the material. The other layer is p-doped and has missing electrons, that can be seen as positively charged holes.
When a current is applied in forward direction, electrons can recombine with holes in the junction area. Electrons from the conduction band, that is energetically higher, fall down to the free places in the energetically lower valence band. In this process, photons with an energy corresponding to the energy gap between the bands are emitted and can cause further stimulated emission in the medium.
To amplify the light further, the semiconductor crystal can also act as a resonator itself, since semiconductor crystals usually have a high refractive index compared to the surrounding air. Therefore, part of the generated light is reflected back into the active medium at the crystal surface perpendicular to the junction plane.
In contrast to LEDs (Light Emitting Diodes) the emitted light of laser diodes is

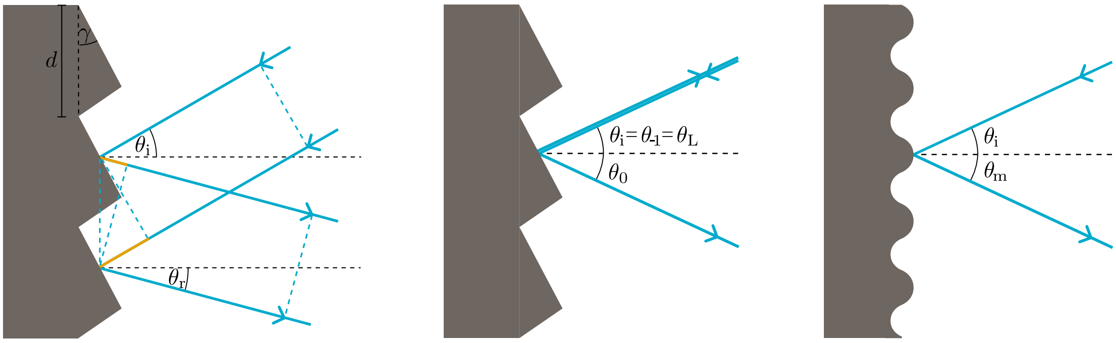

(a) Grating geometry (b) Littrow configuration (c) Holographic grating

Figure 6: Reflective grating surface with incident and reflected light beams. (a) shows the optical path difference of the incoming and reflected beams. (b) shows the angles for Littrow configuration. (c) shows the surface of a holographic grating.

generated not by spontaneous emission but stimulated emission when a certain threshold current is exceeded [22].

2.2.3 External Cavity Diode Lasers in Littrow Configuration

Since the correct wavelength has to be selected to address the transition, the laser wavelength should be tunable. This can be realized with an external cavity constructed with a reflective grating that is hit by the outgoing laser beam.
Figure 6(a) shows a light beam represented by two parallel rays hitting the surface of a blazed grating. This is a special form of reflective grating and is characterized by its groove spacing d, blaze angle γ and the blaze wavelength λ_B, for which the efficiency is maximum for a specific diffraction order. The incoming light beam encloses an angle θ_i with the grating normal while the refracted beam has an angle of θ_r. As highlighted in figure 6(a), the optical path of both rays is different as they are reflected. Equating the path difference Δs of both rays with an integer number of wavelengths $m\lambda$, as required for constructive interference, yields the grating equation

$$\Delta s = d \cdot (\sin(\theta_\mathrm{r}) + \sin(\theta_\mathrm{i})) = m\lambda. \tag{2.3}$$

The order of the refracted beam is given by m. The zeroth order beam with $m = 0$ is diffracted under the incidence angle $\theta_0 = -\theta_\mathrm{i}$.
The Littrow configuration describes a special geometry, where the incoming beam overlaps with the first negative diffraction order as shown in figure 6(b). Thus, both angles are $\theta_\mathrm{i} = \theta_\mathrm{r} = \theta_\mathrm{L}$, with the Littrow angle θ_L given by [23]

$$2d\sin(\theta_\mathrm{L}) = \lambda. \tag{2.4}$$

The highest efficiency can be achieved when the Littrow angle is equal to the blaze angle γ of the grating. While the first negative order is back reflected into the laser diode to provide feedback for stimulated emission, the zeroth order, diffracted under an angle $\theta_0 = \theta_{\mathrm{L}}$, can be used as output beam of the laser [24].
Equation (2.4) also shows that the laser wavelength can be varied if the grating angle is changed slightly. However, this is only possible if the feedback beam is still reflected into the laser diode. Additionally, the efficiency and with it the output power of the laser decreases if the incidence angle deviates too far from the blaze angle of the grating.
In comparison to blazed gratings, holographic gratings have a wave-like shaped cross section. However, they can diffract light according to the same equations as blazed gratings, since they only depend on the groove spacing d and not the groove shape [24]. The cross section of a holographic grating is depicted in figure 6(c).

2.3 Gaussian Beam Optics

An ideal laser beam can be described as a Gaussian beam. The following section reviews the basics of Gaussian beams and is based on [25].

2.3.1 The Gaussian Beam

The laser beam, as an electromagnetic wave, can be described by a complex wave function $U(\vec{r}, t)$. A monochromatic wave with the complex amplitude $U(\vec{r})$ and frequency ν is described by

$$U(\vec{r}, t) = U(\vec{r})\, e^{i2\pi\nu t}. \tag{2.5}$$

A paraxial wave is a wave whose wavefront normals form small angles with the axis of propagation. Such a wave can be described as a plane wave propagating along the z-axis

$$U(\vec{r}) = A(\vec{r})\, e^{-ikz} \quad \text{with} \quad k = \frac{2\pi\nu}{c} = \frac{\omega}{c} \tag{2.6}$$

where $A(\vec{r})$ is a complex envelope that slowly varies with position, k is the wavenumber, c the speed of light and ω the angular frequency. These waves need to satisfy the paraxial Helmholtz equation

$$\nabla_\rho^2 A - i2k\frac{\partial}{\partial z}A = 0 \quad \text{with} \quad \nabla_\rho^2 = \frac{\partial^2}{\partial x^2} + \frac{\partial^2}{\partial y^2}. \tag{2.7}$$

The Gaussian beam is a solution of this equation and is described by a complex envelope

$$\begin{aligned} A(\vec{r}) &= \frac{A_1}{q(z)} \exp\left(-ik\frac{\rho^2}{2q(z)}\right) \\ \text{with} \quad \rho^2 &= x^2 + y^2 \quad \text{and} \quad q(z) = z + iz_0 \end{aligned} \tag{2.8}$$

where A_1 is a constant, ρ the radial coordinate and z_0 is called the Rayleigh length. By splitting $1/q(z)$ in equation (2.8) into its real and imaginary part and using the expression for $U(\vec{r})$ in (2.6) one can derive the complex amplitude

$$U(\vec{r}) = A_0\,\frac{w_0}{w(z)}\,\exp\left(-\frac{\rho^2}{w(z)^2}\right)\exp\left(-ikz - ik\frac{\rho^2}{2R(z)} + i\zeta(z)\right) \tag{2.9}$$

and intensity

$$I(\vec{r}) = |U(\vec{r})|^2 = I_0\left(\frac{w_0}{w(z)}\right)^2 \exp\left(-\frac{2\rho^2}{w(z)^2}\right) \tag{2.10}$$

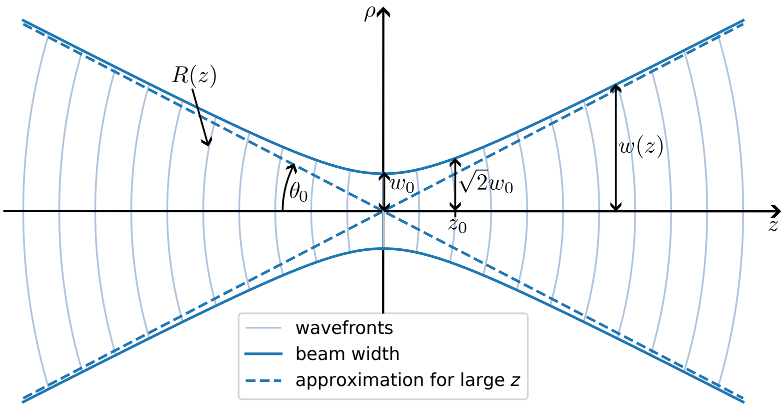

Figure 7: Illustration of a Gaussian beam with the beam radius and the curvature of the wavefronts around the beam waist at $z = 0$.

of the Gaussian beam. The parameters A_0, $w(z)$, $\zeta(z)$, $R(z)$ and w_0 describe different properties of the beam and will be discussed in the following.
As it can be seen in (2.10), the beam intensity in the x-y-plane is described by a Gaussian function. Thus, the radius w of the beam is defined as the distance to the z-axis where this function has decreased to $1/e^2$ of its maximum value. The beam radius has its minimum

$$w_0 = \sqrt{\frac{\lambda z_0}{\pi}} \tag{2.11}$$

in the focus of the beam that is defined at $z = 0$. This is also called the waist radius. For all other distances z to the beam waist the beam radius can be calculated as

$$w(z) = w_0\sqrt{1 + \left(\frac{z}{z_0}\right)^2}. \tag{2.12}$$

As it can be seen from the equation, at the Rayleigh length $z = z_0$ the beam radius has increased to $\sqrt{2}w_0$. For very large distances $z \gg z_0$, the radius increases approximately linear with z. Therefore, the beam takes the shape of a cone with an opening angle of $2\theta_0$ that is inversely proportional to the beam waist w_0. The Gouy phase

$$\zeta(z) = \arctan\left(\frac{z}{z_0}\right) \tag{2.13}$$

describes a phase retardation in comparison to a plane wave that increases from $-\pi/2$ for $z = -\infty$ to $\pi/2$ for $z = \infty$. The parameter

$$R(z) = z\left(1 + \left(\frac{z_0}{z}\right)^2\right) \tag{2.14}$$

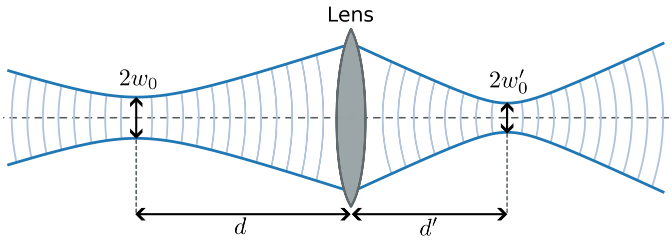

Figure 8: Illustration of a Gaussian beam with beam waist w_0 that is transmitted through a thin lens and focused to another waist w'_0.

is the radius of curvature of the wavefronts at a given distance z. It follows that the wavefronts at the beam waist are planar with an infinite radius of curvature while they have their maximum curvature at $z = z_0$. For $z \gg z_0$, the wavefronts resemble those of a spherical wave with $R(z) = z$. This is also illustrated in figure 7. The shape of a Gaussian beam is characterized only by the independent parameter w_0 and the wavelength λ. All other parameters mentioned above can be calculated from those.

2.3.2 Transmission through a thin Lens

When a thin lens with focal length f is placed in the path of a Gaussian beam with $w(z)$, $R(z)$ and w_0, the transmitted beam can also be described as another Gaussian beam but with different beam parameters. This can be seen in figure 8. As the beam is transmitted through the lens, the width w does not get changed whereas the radius of curvature R is altered according to

$$\frac{1}{R'} = \frac{1}{R} - \frac{1}{f} \tag{2.15}$$

where R' describes the curvature of the wavefronts directly after the lens. As it can be seen from the equation, the sign of R can also change during the transmission. This means that a diverging beam converges after passing the lens and is focused to another waist. If the lens is placed in the beam waist of the incoming Gaussian beam, the new waist

$$w'_0 = \frac{w_0}{\sqrt{1 + \left(\frac{z_0}{f}\right)^2}} = \frac{w_0}{\sqrt{1 + \frac{\pi^2 w_0^4}{\lambda^2 f^2}}} \tag{2.16}$$

is located at a distance

$$d' = \frac{f}{1 + \left(\frac{f}{z_0}\right)^2} \tag{2.17}$$

from the lens [25].

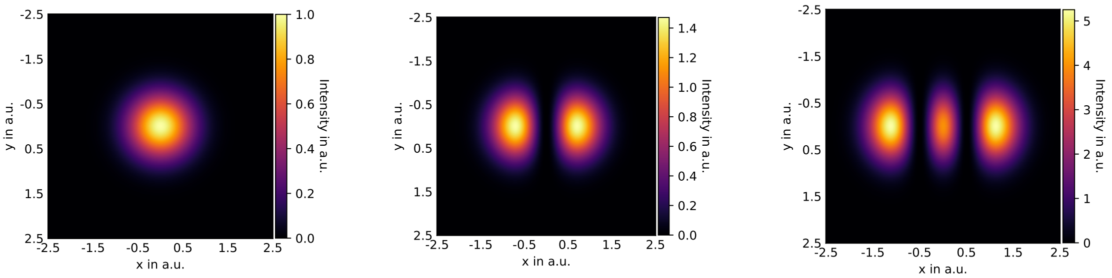

(a) TEM_{00} mode (b) TEM_{10} mode (c) TEM_{20} mode

Figure 9: Intensity distribution $I_{\mathrm{l,m}}(x, y)$ of the Hermite-Gaussian beam for three of the lower transversal electromagnetic (TEM) modes.

2.3.3 Hermite-Gaussian Beams

In addition to the Gaussian beam described before, the Hermite-Gaussian beams are another set of possible solutions for the paraxial Helmholtz equation. They can be derived by modulating the Gaussian beam A_{G} in equation (2.8). The intensity distribution in the plane perpendicular to the z-axis corresponds to a Gaussian function modulated by the Hermite polynomials H_{l} in the x-direction and H_{m} in the y-direction, with the order $l = 0, 1, 2, ...$ and $m = 0, 1, 2, ...$ Thus, all these solutions can be labeled by the indices (l, m). When shifting along the z-axis, the distribution gets only scaled by the factor $w(z)$ like for a Gaussian beam.
The phase of the original Gaussian beam is only changed by a phase $(l + m)\zeta(z)$, that depends on the position z with $\zeta(z)$ defined as in (2.13). Thus, the modulated wave is not a Gaussian beam anymore but shares the Gaussian beam's wavefronts. The intensity distribution of these beams is

$$I_{\mathrm{l,m}}(x, y, z) = |A_{\mathrm{l,m}}|^2 \left(\frac{w_0}{w(z)}\right)^2 G_{\mathrm{l}}^2\left(\frac{\sqrt{2}x}{w(z)}\right) G_{\mathrm{m}}^2\left(\frac{\sqrt{2}y}{w(z)}\right) \tag{2.18}$$

with a constant $A_{\mathrm{l,m}}$ and the Hermite-Gaussian function of order l

$$G_{\mathrm{l}}(u) = H_{\mathrm{l}}(u) \cdot e^{-\frac{u^2}{2}}. \tag{2.19}$$

Four of the lower modes in the x-y-plane, are shown in figure 9 as an example. As it can be seen in figure 9(a), the intensity distribution $I_{0,0}$ corresponds to that of an unmodulated Gaussian beam. The indices l and m then describe the number of nodes along the x- and y-axis. With increasing indices, the spatial extent of the different beams in the x- and y-direction is increasing as well.

2.4 Laser Locking using Transfer Cavities

The frequency of each laser in an experiment with cold atoms or molecules needs to be kept stable. In our group we utilize a scanning transfer cavity lock, which was developed by Einius Pultinevicius [26]. This section introduces the basics of Fabry-Perot interferometers as well as the principle of scanning transfer cavity locking.

2.4.1 Fabry-Perot Interferometer

A Fabry-Perot interferometer is an optical device that only transmits certain light frequencies. It consists of two plane mirrors that are aligned parallel to each other, forming a resonator with length L. The inner surfaces of both mirrors have a high reflectivity $\tilde{R}$ while the outer surfaces are highly transparent. This ensures that only the inner surfaces of the mirrors contribute to the resonator [27].
A light beam with wavelength λ entering this cavity is reflected back and forth between the mirrors. Every time the light passes one mirror a fraction of the light is transmitted out of the cavity. Behind the second mirror, all transmitted waves interfere with each other. The phase difference between a transmitted light wave in comparison to a wave that has taken one round-trip more in the resonator is $\Delta\phi = 2Ln \cdot 2\pi/\lambda$ for an incidence angle of $0°$ and a material with refractive index n between the mirrors. All partially transmitted waves interfere constructively, if $\Delta\phi = 2m\pi$ with an integer m. Thus, the total transmitted intensity shows maxima for the frequencies

$$\nu_m = \frac{c}{\lambda_m} = \frac{mc}{2nL}. \tag{2.20}$$

The frequency distance

$$\delta\nu = \nu_{m+1} - \nu_m = \frac{c}{2nL} \tag{2.21}$$

between two adjacent peaks is called free spectral range (FSR) of the resonator. The full width at half maximum of one of the transmission peaks is

$$\Delta\nu = \frac{c}{2nL} \cdot \frac{1-\tilde{R}}{\pi\sqrt{\tilde{R}}}. \tag{2.22}$$

The ratio of both is the finesse

$$\mathcal{F} = \frac{\delta\nu}{\Delta\nu} = \frac{\pi\sqrt{\tilde{R}}}{1-\tilde{R}} \tag{2.23}$$

and describes the number of different light waves that interfere with each other or how often the light is reflected inside the cavity before leaving it. The transmitted

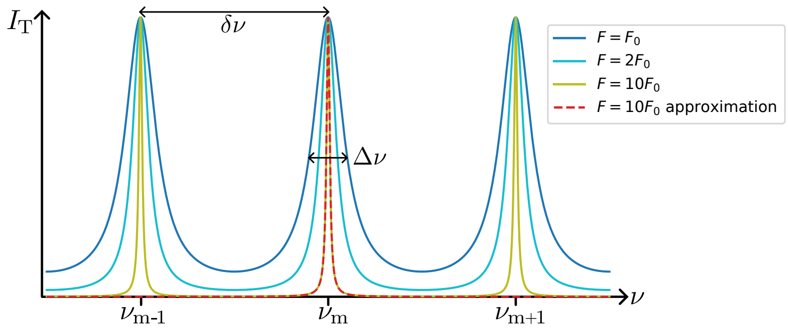

Figure 10: Transmission curve of a Fabry-Perot interferometer for different values of the finesse and approximation of one single peak as Lorentz profile.

intensity as a function of frequency is

$$I_T(\nu) = \frac{I_{max}}{1 + \left(\frac{2\mathcal{F}}{\pi}\right)^2 \sin^2\left(\frac{\pi\nu}{\delta\nu}\right)} \tag{2.24}$$

and is also depicted in figure 10 [27].
It can be seen in the transmission curve that the transmission peaks are sharper and more separated from each other for a higher finesse of the cavity. To describe a single transmission peak located at $\nu = 0$ for frequencies close to its maximum, the sine function can be approximated by its argument. Therefore a single peak

$$I_T(\nu) \approx \frac{I_{max}}{1 + \left(\frac{2\mathcal{F}\nu}{\delta\nu}\right)^2} \tag{2.25}$$

can be described by a Lorentz function [25].

2.4.2 Spherical Mirror Resonator and Mode Matching

For higher stability, a cavity can also consist of two curved mirrors with radii R_1 and R_2, placed at positions z_1 and z_2 with a distance L between them. For the resonator to be stable, the condition

$$0 \leq \left(1 - \frac{L}{R_1}\right)\left(1 - \frac{L}{R_2}\right) \leq 1 \tag{2.26}$$

has to be fulfilled by the resonator geometry [28].
A Gaussian beam is reflected back on itself at one of the mirrors if the curvature of the wavefront matches the curvature of the mirror. If this condition is fulfilled at both mirrors and the phase of the light does only change by an integer number of

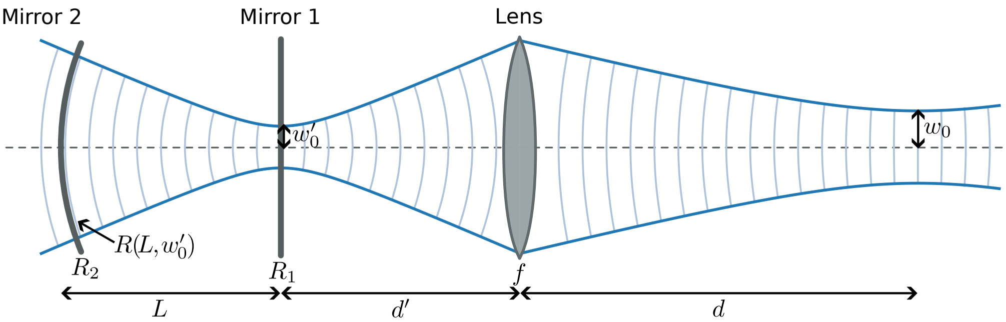

Figure 11: Schematic of a Gaussian beam coupled into a plano-concave resonator by focusing it with a lens.

$\pm 2\pi$ during one round trip, the Gaussian beam is a mode of the resonator. Since Hermite-Gaussian beams share the wavefronts of the Gaussian beam, they can also match the curvatures of the spherical mirrors and can therefore be resonator modes [25].
Since the Hermite-Gaussian intensity distributons with $(l, m) \neq (0, 0)$ do not show a rotation symmetry around the optical axis, they can mainly occur when the cavity mirrors are not aligned perfectly, which breaks this symmetry. For a Hermite-Gaussian beam of order (l,m), the resonance frequencies of the resonator modes are

$$\nu_{\mathrm{l,m,q}} = q\nu_{\mathrm{F}} + (l + m + 1)\frac{\Delta\zeta}{\pi}\nu_{\mathrm{F}} \quad \text{with} \quad \nu_{\mathrm{F}} = \frac{c}{2L} \tag{2.27}$$

and $q = 0, \pm 1, \pm 2, ...$ Modes with the same (l,m) which only differ in index q are called longitudinal modes, while different indices (l,m) indicate transverse modes of the resonator. Two adjacent longitudinal modes of the same transverse mode have a frequency spacing of

$$\nu_{\mathrm{l,m,q+1}} - \nu_{\mathrm{l,m,q}} = \nu_{\mathrm{F}}, \tag{2.28}$$

which is the same result as for the FSR $\delta\nu$ of the Fabry-Perot interferometer described in the previous section [25].
The optical setup presented in this thesis includes a plano-concave cavity where $R_1 = \infty$. The laser beam is coupled into the resonator by using a lens with a focal length f. A schematic of this situation is depicted in figure 11. For the highest coupling efficiency, the curvature of the wavefronts, given by equation (2.12), has to match the mirror curvatures. In case of a plano-concave cavity, the focus with w_0' after the lens has to be at the first plane mirror. For a given mirror radius R_2, the required z_0' can then be calculated by solving equation (2.12) for z_0 and inserting $z = L$. With equation (2.11) this leads to

$$w_0' = \sqrt{\frac{\lambda L}{\pi}} \cdot \sqrt[4]{\frac{R_2}{L} - 1} \tag{2.29}$$

for the required beam waist. If the incoming beam is approximately collimated, the focal length f of the lens can be derived using equation (2.15).

2.4.3 Laser Locking with a Scanning Transfer Cavity

As the transmission frequency of a cavity is a function of its length, the transmission curve of the cavity can be recorded by varying the cavity length L for a constant light frequency. This can be done by shifting the position of one mirror with a piezo crystal. The piezo actuator changes its length approximately linearly with the applied voltage. The cavity length can thus be controlled by the applied piezo voltage. Therefore, a single laser with constant frequency causes a series of peaks like shown in figure 10 while the cavity length is increasing or decreasing as a function of time.

Fluctuations or drifts of the transmission peaks can occur due to external influences that affect the optical length of the cavity such as temperature or air pressure. However, the peaks of two different lasers transmitted through the same cavity are affected by these fluctuations in the same way. So their relative distance in the transmission curve can only vary due to frequency drifts of the lasers.

Such a cavity will be used for frequency locking of the diode lasers. To stabilize the diode laser frequency, the distance between the peaks caused by the diode laser and the respective peaks of a reference laser is kept constant. However, the reference laser requires a very stable frequency, since all fluctuations of the reference laser will also shift the diode laser frequency. In our experiment, we use a helium-neon laser as a reference laser.

2.5 Electro-Optics

Laser frequencies can either be modulated by acousto-optical modulators (AOMs) or electro-optical modulators (EOMs). In the setup for this thesis, the frequency spectrum of a diode laser is manipulated using an electro-optical phase modulator. The following section gives a brief summary of phase modulation and its applications.

2.5.1 Phase Modulators

In an electro-optic medium, the refractive index n depends on an applied electric field E. Under the condition that E is slowly varying in comparison to light frequencies, the refractive index can be written as

$$n(E) \approx n + a_1 E + \frac{a_2}{2} E^2 + ... \tag{2.30}$$

with $n = n(0)$ and the coefficients

$$a_1 = \frac{\mathrm{d}n}{\mathrm{d}E}\bigg|_{E=0} \quad \text{and} \quad a_2 = \frac{\mathrm{d}^2 n}{\mathrm{d}E^2}\bigg|_{E=0}. \tag{2.31}$$

Higher orders of this expansion are typically very small compared to n and can therefore be neglected. For specific materials even the third term proportional to E^2 can be neglected [25]. Such a material is for example lithium niobate ($LiNbO_3$) crystal, that is contained in the phase modulator used for the measurements [29]. The effect of the refractive index changing linearly with E is called Pockels effect. The phase of a light beam can be modulated with a phase modulator as depicted in figure 12. A time dependent voltage $V(t)$ is applied between two electrodes of length L with a gap g between them, inducing an electric field $E = V/g$. Between the electrodes, the light propagates through a waveguide that is applied on a substrate [25].
By varying the refractive index of the medium the light is travelling through, the optical path $n(E)L$ changes as well. This leads to a phase shift of

$$\phi_{\text{tot}} = n(E)k_0 L \approx n k_0 L + a_1 E k_0 L = n k_0 L + \phi(t) \tag{2.32}$$

where k_0 is the wavevector of the light in free space. Therefore, one can modulate the phase by varying the applied driving voltage.
The half-wave voltage V_π is defined as the voltage that leads to an additional phase shift of $\phi(t) = \pi$. Thus, a peak-to-peak voltage of $V_{\text{pp}} = 2V_\pi$ is required to achieve the full modulation depth of 2π [25]. The modulation depth is given by [30]

$$\beta = \frac{|\phi(t)_{\text{max}} - \phi(t)_{\text{min}}|}{2\pi}. \tag{2.33}$$

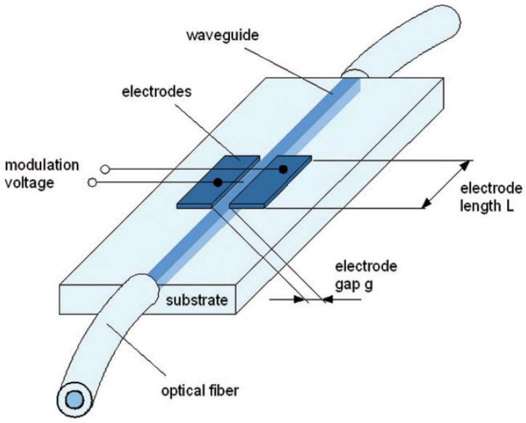

Figure 12: Schematic setup of a fiber coupled phase modulator. Figure taken from [29].

2.5.2 Sinusoidal Modulation

Symmetric sidebands of the initial light frequency ω_0 can be created by choosing the driving voltage to be a sinusoidal signal with frequency Ω. A light wave that has passed through the phase modulator and has accumulated an additional phase shift of $\phi(t)$ can be described as

$$E_\mathrm{m}(t) = \mathrm{Re}\left[E_0 e^{i\omega_0 t + i\phi(t)}\right] = \mathrm{Re}[E_0 e^{i\omega_0 t} \cdot e^{i\phi_0 \sin(\Omega t)}]. \tag{2.34}$$

Since the last term is periodic with a periodicity of $T = 2\pi/\Omega$, it can be written as a Fourier series

$$e^{i\phi_0 \sin(\Omega t)} = \sum_{l=-\infty}^{\infty} C_l \cdot e^{il\Omega t} \tag{2.35}$$

with the Fourier coefficients

$$C_l = \frac{\Omega}{2\pi} \int_{-\pi/\Omega}^{\pi/\Omega} e^{i\phi_0 \sin(\Omega t)} e^{-il\Omega t} \mathrm{d}t. \tag{2.36}$$

By substituting $u = \Omega t$, one can show that the Fourier coefficients are given by the Bessel functions $C_l = J_l(\phi_0)$ of order l. Inserting this result into equation (2.34) yields the light wave

$$E_\mathrm{m}(t) = \mathrm{Re}\left[E_0 \sum_{l=-\infty}^{\infty} J_l(\phi_0) e^{i(\omega_0 + l\Omega)t}\right] \tag{2.37}$$

after phase modulation. It is represented by a sum of waves with different frequencies. In addition to the carrier frequency ω_0 of the incoming light, the frequency spectrum features symmetric sidebands with frequencies $\omega_0 + l\Omega$. The heights of these peaks are described by the squared Bessel functions $J_l(\phi_0)^2$ and thus a function of the applied voltage amplitude. Using equation (2.33), the modulation depth of for the sinusoidal modulation is [30]

$$\beta = \frac{|\phi_0|}{\pi} = \frac{V_{\mathrm{pp}}}{2V_\pi}. \tag{2.38}$$

2.5.3 Serrodyne Modulation

Sequences of voltage ramp signals can be used to create arbitrary spectra. This is very useful for applications in atomic physics experiments where the hyperfine splitting of an atomic or molecular species has to be covered, since these splittings are in general not symmetric.
A phase shift of $\phi(t) = \alpha t$ that changes linearly with time leads to a modulated light wave with

$$E_{\mathrm{m}}(t) = \mathrm{Re}\left[E_0 e^{i(\omega_0+\alpha)t}\right]. \tag{2.39}$$

Hence, the carrier frequency gets shifted according to the gradient α. Since one cannot apply a constantly rising voltage for any length of time, a periodic sawtooth voltage with a specific gradient is utilized to create the frequency shift. Several different frequency sidebands can be created by adding intervals of different ramp gradients that each correspond to one of the shifted frequencies.

3 Experimental Setup

The optical setup for the measurements is divided in four parts. The construction of the external cavity diode laser that will be used as a second repump laser is described in section 3.1. The output of this laser is coupled into three different optical fibers. The setup for this is shown in section 3.2. A similar setup is used for fiber coupling of the first repump laser, which is shown in section 3.3. Finally, both repump lasers as well as a helium-neon-laser are coupled in two cavities for frequency locking, which is described in section 3.4.

3.1 Construction of the Second Repump Laser

The second repump laser is an external cavity diode laser in Littrow configutation as described in section 2.2.3. The design of this laser system was already used at our institute. The semiconductor laser diode is a Toptica LD-0633-0100-1 diode with an anti-reflection coating on its casing to prevent the formation of an additional resonator with this interface. Laser diodes are not typically fabricated for the required wavelength of $\lambda = 628.1\,\mathrm{nm}$ and sufficient output power can typically only be achieved by using complex leader-follower set-ups that need to be cooled to low temperatures [17]. The laser diode used for this laser has a typical lasing wavelength of $\lambda = 634.0\,\mathrm{nm}$ according to its data sheet. However, the diode was selected to operate closer to the required wavelength. This special diode is specified with a center wavelength of $\lambda = 630.8\,\mathrm{nm}$ [31]. Although it was not guaranteed that a laser with this diode can achieve the correct wavelength, it is shown in this thesis that it can, under the right conditions, indeed operate at 628.1 nm.
The laser setup is shown in figure 13. The numbers in brackets in the following refer to the numbers depicted in this image. The laser diode is placed inside an adjustable collimation tube[1] (2). This holder also contains a collimation lens that focuses the divergent light from the diode. The distance between the laser diode and the lens is adjusted to shift the focus of the light beam as far away as possible in order to get an approximately collimated beam. This beam is diffracted at the grating (3), which is a reflective holographic grating[2] with 1800 grooves/mm and a wavelength range of 400 to 700 nm.
The grating is glued to the front plate of a holder (6). The incidence angle of the light beam can be varied with a micrometer screw (5) for coarse adjustment and a piezo actuator[3] (4) for fine tuning. Turning the screw or applying a voltage to the piezo can bend the front plate away from the holder to change the grating

[1] Thorlabs LTN330
[2] Edmund Optics 43-775
[3] Thorlabs PK2JAP1

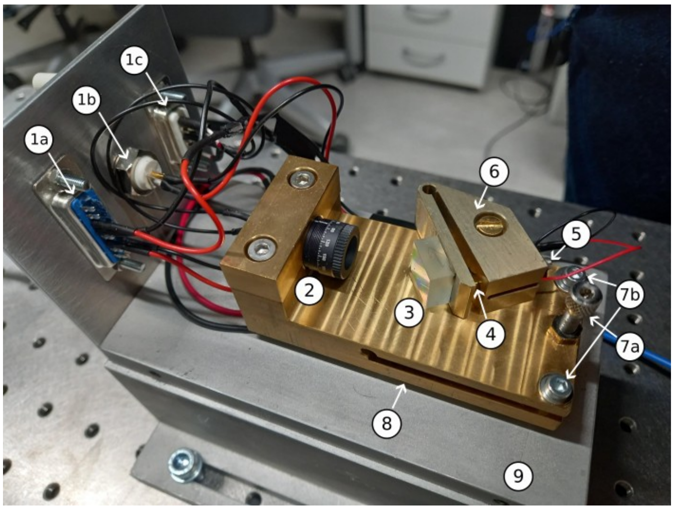

Figure 13: Inner setup of the second repump laser in Littrow configuration. The numbered components are: (1a, b, c) ports for temperature, piezo voltage and diode current controller, (2) diode holder with collimation lens, (3) grating, (4) piezo actuator, (5) micrometer screw, (6) grating holder, (7a, b) screws for adjustment of grating position, (8) Peltier element, (9) base block.

angle. Both, the diode holder and the grating holder are placed on a base plate whose upper plate can be bent upward by a micrometer screw (7a) or bent down by the screws (7b) in order to adjust the grating angle. The base plate is placed on a base block (9) with a Peltier element (8) between them to control the diode temperature. When a current is applied to the peltier element, one side gets colder while the other side gets warmer. Thus, the base block also acts as a heat sink. A thermistor[4] at the side of the base plate measures the temperature of the laser.
The peltier element together with the thermistor, the piezo actuator and the laser diode are connected to respective ports (1a), (1b) and (1c) in the case of the laser that are connected to a temperature controller[5], power supply[6] and a laser diode controller[7] respectively. The temperature controller records the resistance of the thermistor and applies a current to the peltier element in order to adjust the recorded value of the thermistor resistance to a set value with a PID loop.
Since the maximum operating current of the laser diode is 170.0 mA according to the datasheet [31], the current limit of the laser diode controller is set to $I_{\text{lim}} = 165.00\,\text{mA}$.

[4]NTC 151-237
[5]Thorlabs TED200C
[6]Elektro-Automatik EA-PS 3016-10 B
[7]Thorlabs LDC202C

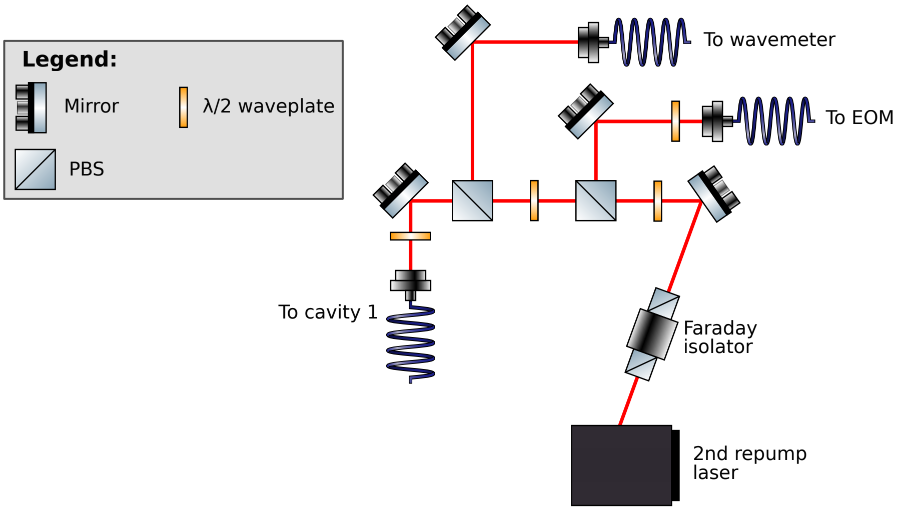

Figure 14: Schematic of the optical setup for fiber coupling of the second repump laser.

The grating holder is approximately positioned under the Littrow angle

$$\theta_{\mathrm{L}} = \arcsin\left(\frac{\lambda}{2d}\right) = \arcsin\left(\frac{628.1\,\mathrm{nm}}{2\cdot\frac{1\,\mathrm{mm}}{1800}}\right) \approx 34.4°. \tag{3.1}$$

However, the exact position is found by varying the grating angle in order to achieve the required wavelength and then maximize the output power. After finishing the adjustments of the grating angle, a casing with an opening for the laser beam is mounted on the laser in order to protect it from external influences like air fluctuations or dust.

3.2 Fiber Coupling of the Second Repump Laser

The optical components in the following parts of the setup are all placed on an optical table that will later be encased to prevent the laser light from getting into the rest of the lab. All the laser beams run approximately parallel to the table surface and on a height of about 10 cm.
The aim of this part of the setup, shown in figure 14, is to couple the laser beam of the second repump laser into three different optical fibers. After leaving the laser, the beam first passes an optical isolator. It prevents light that is reflected at the optical components to get back into the laser. However, the power of the laser beam gets reduced to approximately 60 % when propagating through the optical isolator.
Next, the laser beam passes two $\lambda/2$-waveplates with a polarizing beam splitter

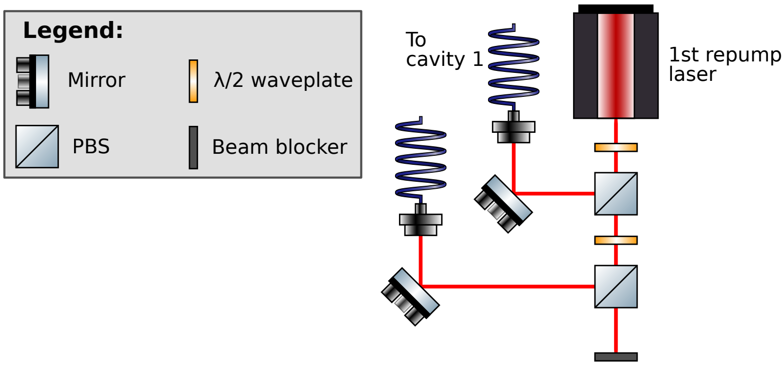

Figure 15: Schematic of the optical setup for fiber coupling of the first repump laser.

(PBS) cube behind each of them. When passing the $\lambda/2$-plates, the polarization axis of the linearly polarized light is rotated around a specific angle, determined by the angle of the waveplate. At each PBS, the vertically polarized part of the light is reflected and the horizontally polarized part is transmitted. Thus, the laser beam is split into three beams whose intensities can be controlled by varying the angles of the waveplates.
All three beams are reflected on a mirror into a fiber coupler. These are placed in a kinematic mount and contain a lens with a focal length of $f = 11\,\mathrm{mm}$. The angles of both the fiber coupler and the mirror in horizontal and vertical direction can be adjusted in order to couple the beam into the optical fiber.
The beam reflected at the first PBS is coupled into a fiber connected to a phase modulator[8] that is used to add sidebands to the laser frequency. Since the output power after the modulator depends on the polarization of the incoming light, an additional $\lambda/2$-waveplate is placed before the fiber coupler, that leads to the phase modulator. The light reflected at the second PBS is coupled into the fiber that leads to a wavemeter. The remaining part of the laser beam is outcoupled again in order to couple it into the cavity for frequency locking.
All the lenses and mirrors are either A or B coated, since the laser wavelength lies in the overlap of both wavelength ranges. The $\lambda/2$-waveplates are specified for a wavelength of 628 nm.

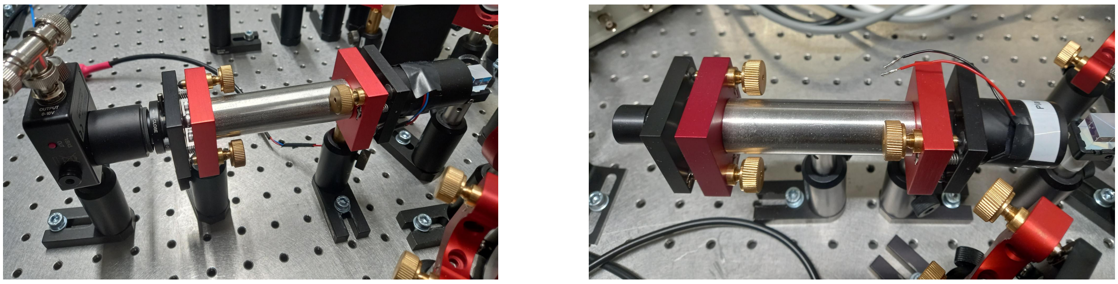

(a) Cavity 1 (b) Cavity 2

Figure 16: Plano-concave cavities for frequency locking.

3.3 Fiber Coupling of the First Repump Laser

The first repump laser consists of a commercial diode laser[9] in Littrow configuration as a seed laser, that is first amplified by a visible Raman fiber amplifier and then frequency-doubled in the outcoupler. The wavelength of the seed laser is $\lambda = 1257.2\,\text{nm}$ and becomes $\lambda = 628.6\,\text{nm}$ after the frequency-doubling stage, as required for the according molecular transition.
The aim of this part of the setup is to couple the first repump laser into two optical fibers. The structure is similar to the previous section and shown in figure 15.
No optical isolator is placed behind the laser, since there is an isolator built into the laser. One of the fibers, that the laser beam is coupled into, leads to the cavity for frequency locking. The other can be connected to a wavemeter. The third part of the laser beam can later be used for a setup on the same optical table.

3.4 Cavities for Frequency Locking

The two plano-concave resonators used for frequency locking are shown in figure 16. Since the construction of both cavities is the same, they will be refered to as cavity 1 and cavity 2 in the following. Cavity 1 is shown in figure 16(a) and cavity 2 in figure 16(b).
The curved mirror has a radius of $R_2 = 20\,\text{cm}$. Both mirrors of a cavity are placed on a mirror mount so that their angle can be adjusted in horizontal and vertical direction. The mirrors are connected by a tube with a distance of $L = 15\,\text{cm}$ between them. The space between the mirrors is filled with air with a refractive index of $n \approx 1$.
The data sheet of the mirrors lists a reflectivity of $\tilde{R} = 99.5\,\%$ for both. How-

[8] Jenoptik PM635
[9] Toptica DL pro

ever, in the experiment it turned out that the width of the transmitted intensity peaks is larger than expected from the cavity's resolution and the linewidth of the laser. Therefore, the reflectivity was measured at the 4th Institute of Physics as a function of the wavelength, which is shown in figure 34 and 35 of the appendix. According to these measurements, the reflectivity at 628 nm is $\tilde{R}_\mathrm{p} = 98.901\,\%$ for the plane mirror and $\tilde{R}_\mathrm{c} = 98.397\,\%$ for the curved mirror. According to the equations (2.21) and (2.22), the cavities have a free spectral range of

$$\delta\nu = \frac{c}{2nL} = \frac{3 \cdot 10^8\,\mathrm{m/s}}{2 \cdot 15\,\mathrm{cm}} = 1\,\mathrm{GHz}$$

and a full width at half maximum of

$$\Delta\nu = \frac{c}{2nL} \cdot \frac{1 - \sqrt{\tilde{R}_\mathrm{p}\tilde{R}_\mathrm{c}}}{\pi\sqrt[4]{\tilde{R}_\mathrm{p}\tilde{R}_\mathrm{c}}} = \frac{3 \cdot 10^8\,\mathrm{m/s}}{2 \cdot 15\,\mathrm{cm}} \cdot \frac{1 - \sqrt{0.98901 \cdot 0.98397}}{\pi\sqrt[4]{0.98901 \cdot 0.98397}} \approx 4.331\,\mathrm{MHz}.$$

With equation (2.23), this corresponds to a finesse of

$$\mathcal{F} \approx 231.$$

However, these values only hold if the mirrors are also aligned perfectly. According to a measurement analogous to those in section 4.1.4, the incoming beam of the second repump laser has a waist of $w_0 = 3.15 \cdot 10^{-4}\,\mathrm{m}$ and is approximately collimated after being outcoupled. As described in section 2.4.2, the required beam waist behind the focusing lens is

$$w_0' = \sqrt{\frac{\lambda L}{\pi}} \cdot \sqrt[4]{\frac{R}{L} - 1} = \sqrt{\frac{628.1\,\mathrm{nm} \cdot 15\,\mathrm{cm}}{\pi}} \cdot \sqrt[4]{\frac{20\,\mathrm{cm}}{15\,\mathrm{cm}} - 1} \approx 1.316 \cdot 10^{-4}\,\mathrm{m}$$

according to equation (2.29) and the required focal length of the lens according to (2.16) is

$$f = \frac{w_0^2\pi}{\lambda\sqrt{\left(\frac{w_0}{w_0'}\right)^2 - 1}} = \frac{(3.15 \cdot 10^{-4}\,\mathrm{m})^2\pi}{628.1\,\mathrm{nm} \cdot \sqrt{\left(\frac{3.15 \cdot 10^{-4}\,\mathrm{m}}{1.316 \cdot 10^{-4}\,\mathrm{m}}\right)^2 - 1}} \approx 228.212\,\mathrm{mm}.$$

Therefore, a lens with $f = 250\,\mathrm{mm}$ is chosen.
The plane mirror of the cavity is connected to a piezo actuator which can shift the mirror position in order to vary the cavity length. The piezo's pins are connected to an arbitrary waveform generator[10] and a ramp voltage is applied to scan the cavity.

[10] Rigol DG1022

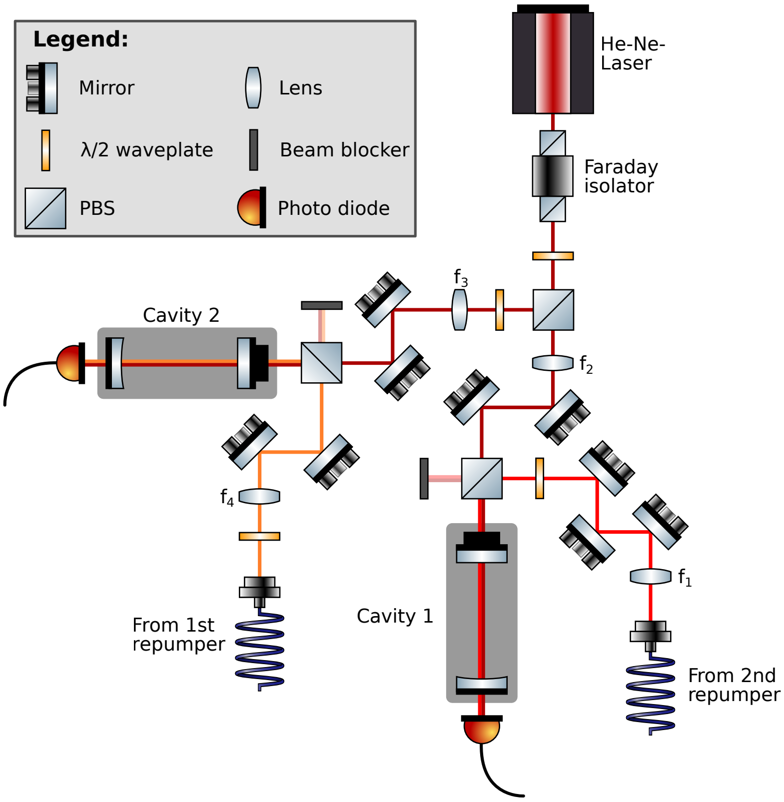

Figure 17: Schematic of the optical setup for coupling the first and second repump laser as well as a helium-neon laser in two cavities for frequency locking.

An aperture is placed behind the concave mirror. With the aperture and a removable pinhole at the plane mirror, a laser beam entering the cavity can be adjusted in a way that it crosses both mirrors centrally. Behind the aperture, a photodiode is set up to record the transmitted intensity. The voltage ramp and the output of the photodiode are observed on an oscilloscope.
A schematic of all optical components in the setup is shown in figure 17. The reference for laser locking is a stabilized helium-neon laser[11]. The laser beam from this laser first passes an optical isolator and then propagates through a $\lambda/2$-waveplate and a PBS where it is split into two parts.
The transmitted part passes a lens with focal length $f_2 = 200\,\mathrm{mm}$ and is reflected at two mirrors. Next, it propagates through a PBS. But since it is polarized horizontally after being transmitted at the first PBS, it is also transmitted at this PBS. Light leaving the PBS in the direction of a reflection is absorbed by a beam block. Behind the PBS, the laser beam passes the first plane mirror of cavity 1. The lens

[11]SIOS Meßtechnik, Serie SL 04

is placed approximately one focal length in front of cavity 1. Hence, the beam is focused at the plane mirror. The focal length is chosen so that the condition for mode matching is fulfilled and the beam can be coupled into the cavity.
The beam part of the helium-neon laser that is reflected at the first PBS behind the optical isolator is coupled into cavity 2 in the same way. The only difference is, that it passes an additional $\lambda/2$-waveplate before the lens with focal length $f_3 = 200\,\mathrm{mm}$. This waveplate is required to rotate the polarization axis of the light by $90°$, since it is reflected at the first PBS but transmitted at the second one in its path before cavity 2.
The part of the light from the second repump laser that is coupled into cavity 1 passes through a lens with focal length $f_1 = 250\,\mathrm{mm}$, is reflected at three mirrors and then propagates through a $\lambda/2$-waveplate. Next, the beam is reflected at the PBS into cavity 1. The waveplate is used to adjust the polarization axis of the light, so that the light entering the cavity is maximized and the part transmitted at the PBS and absorbed at the beam block is minimized. The lens is placed one focal length in front of the cavity. Two mirrors are used to adjust be beam inside the cavity.
The light from the first repump laser is coupled into cavity 2 in the same way. The lens used for coupling the beam into the cavity, has a focal length of $f_4 = 200\,\mathrm{mm}$. The only difference is that the beam is reflected at only two mirrors, which are sufficient for the adjustment of the beam path.
It is possible to expand this setup by adding another PBS before both cavities. Since the cooling laser and the slowing laser also need to be frequency locked, they can be coupled on cavity 1 and 2 in addition to the other lasers.

4 Results

4.1 Characterization of the Second Repump Laser

4.1.1 Wavelength Spectrum of the Laser Diode

The laser diode used for the second repump laser has a typical lasing wavelength of $\lambda = 630.8\,\mathrm{nm}$ according to its data sheet. As this deviates from the required wavelength of $\lambda = 628.1\,\mathrm{nm}$, the laser diode wavelength is recorded in a first measurement. The output beam of the laser diode without an external resonator is coupled into a fiber and connected to the wavemeter. The wavelength is recorded over approximately one minute for different currents applied to the laser diode. Figure 18 shows the spectra for $I = 73\,\mathrm{mA}$ and $I = 155\,\mathrm{mA}$. Both show a maximum emission wavelength, which corresponds to the band gap in the semiconductor material. The laser diode can emit photons with energies larger than the band gap and smaller wavelengths. However, it cannot emit photons with energies smaller that the band gap, which is the reason why the emission spectrum breaks off at this wavelength.
For the lower current, the diode mainly emits at about 629.3 nm but there is also emission at 628.1 nm. Figure 18(b) shows that the maximum emission wavelength increases for increasing diode current. The laser diode is mainly emitting at $\lambda = 631.2\,\mathrm{nm}$. With this results it seems possible to operate the laser at the required wavelength, however only for low diode currents with an external resonator to tune the wavelength.

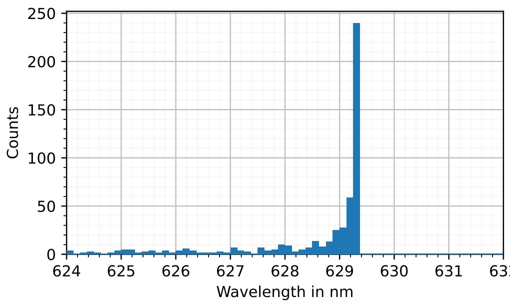

(a) Spectrum for $I = 73\,\mathrm{mA}$

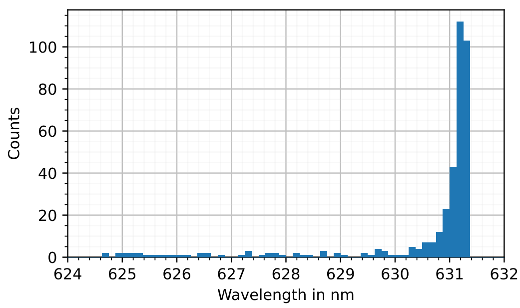

(b) Spectrum for $I = 155\,\mathrm{mA}$

Figure 18: Spectra for the output of the laser diode without grating. The histograms are recorded for two different diode currents and show that it is possible to operate the diode laser with an external cavity at the required wavelength of 628 nm.

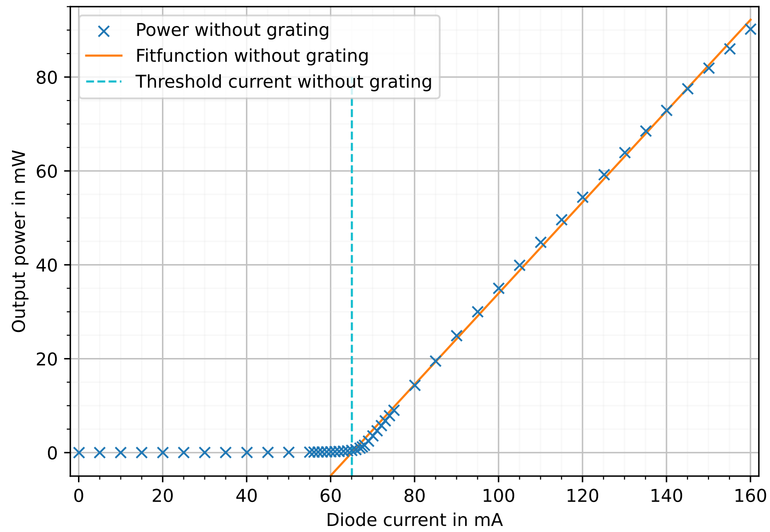

Figure 19: The output power of the laser diode as a function of the current recorded without the grating shows the typical characteristic of a diode. A linear function is fitted to the data with a linear increase to determine the threshold current $I_{\mathrm{th}} = 65.1\,\mathrm{mA}$ and the slope efficiency $m = 0.971\,\mathrm{W/A}$.

4.1.2 Output Power Curve

Figure 19 shows the output power of the laser diode as a function of the current. The characteristic power curve is recorded without an external resonator for currents lower than 160 mA, since the maximum operation current of the laser diode is 170 mA. Even without an external resonator the diode can emit laser light and shows the characteristic behaviour of a diode. For low currents, the emitted light only results from spontaneous emission and has a low output power. When the current reaches a threshold current I_{th}, the stimulated emission begins to dominate and the output power increases linearly with the current. The gradient of this linear curve is the slope efficiency m. Hence, the function

$$P_{\mathrm{fit}}(I) = m(I - I_{\mathrm{th}}) \tag{4.1}$$

is fitted to the recorded data to determine the threshold current $I_{\mathrm{th}} = 65.1\,\mathrm{mA}$ and the slope efficiency $m = 0.971\,\mathrm{W/A}$. The data sheet gives a threshold current of $I_{\mathrm{th}} = 68.99\,\mathrm{mA}$ at a temperature of 25 °C [31], which is higher than the recorded value. However, the measurement was recorded at a room temperature of 21 °C without a temperature controller. Since the threshold current of laser diodes typically increases for increasing temperature [28], this result is in agreement with the

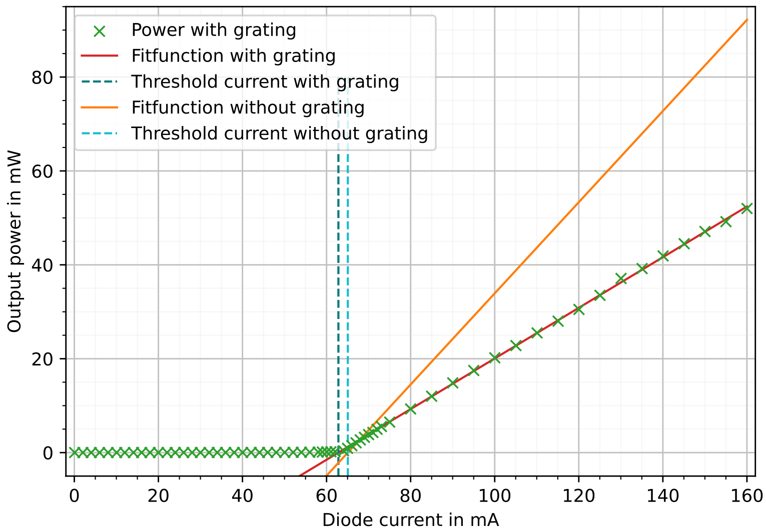

Figure 20: Output power of the laser diode as a function of the diode current recorded with the grating. A linear function is fitted to the data that shows a linear increase to determine the threshold current $I_{\mathrm{th}} = 62.8\,\mathrm{mA}$ and the slope efficiency $m = 0.539\,\mathrm{W/A}$. Both the threshold current and the slope efficiency have decreased in comparison to the results without the grating. For clarity, the fit function for the case without the grating is also included in the plot.

data sheet.
In the next step, the grating is added to the laser diode as an external resonator to adjust the wavelength. The exact grating position is found by varying the grating angle with the micrometer screw on the grating holder in order to get close to the required wavelength of 628.1 nm. It is necessary to turn the grating to the edge of the range where the reflected light still gives feedback to the laser diode. Therefore, the output power is not as high as possible for other wavelengths. With this fixed grating position, the other screws on the base plate of the laser are used to lower the lasing threshold as far as possible.
Figure 20 shows the power curve of the laser with an external resonator. It was recorded for a NTC resistance of $R = 13.260\,\mathrm{k\Omega}$ which corresponds to a temperature of $T = 18.8\,°\mathrm{C}$. The curve also shows the typical behaviour of a diode and is fitted with the function in equation (4.1). Since the grating gives additional feedback to the laser diode, the threshold current has decreased to $I_{\mathrm{th}} = 62.8\,\mathrm{mA}$. However, the output power has been lowered too. The slope efficiency $m = 0.539\,\mathrm{W/A}$ is 55.51 % of the value without the grating.

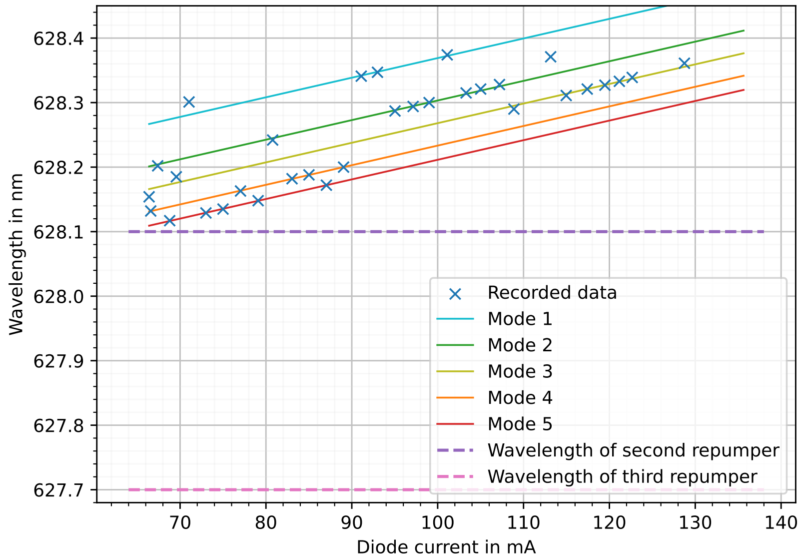

Figure 21: Wavelength of the second repump laser as a function of the diode current for a constant temperature of $T = 18.8\,°\mathrm{C}$. Different modes are shown as parallel lines with a gradient of $0.003\,\mathrm{nm/mA}$. The plot also shows the wavelengths of the second and third repump transitions. It shows that it is possible to achieve the required wavelength for the second repump transition but not for the third.

4.1.3 Wavelength as Function of Current and Temperature

For a fixed grating position, the laser's wavelength also depends on the diode current and temperature. The temperature is not measured directly. Instead, the temperature controller records the resistance of the NTC and can also set it to a certain value. The resistance can then directly be converted into a temperature by using equation 6.1.

Figure 21 shows the wavelength recorded as a function of the current for a constant NTC resistance of $R = 13.264\,\mathrm{k\Omega}$, which corresponds to a temperature of $T = 18.8\,°\mathrm{C}$. The wavelength increases linearly with increasing current. However, the wavelength jumps between different modes that differ in the number of wave nodes inside the resonator. In this measurement one can distinguish five modes with more than two data points. These are indicated by fitted lines in the plot. All the modes have approximately the same gradient of $0.003\,\mathrm{nm/mA}$.

In this measurement, lots of jumps between the different modes occur. This is partly due to the fact, that it was recorded without the casing of the laser. If the casing is mounted, the laser is less unstable and can be operated in one mode for

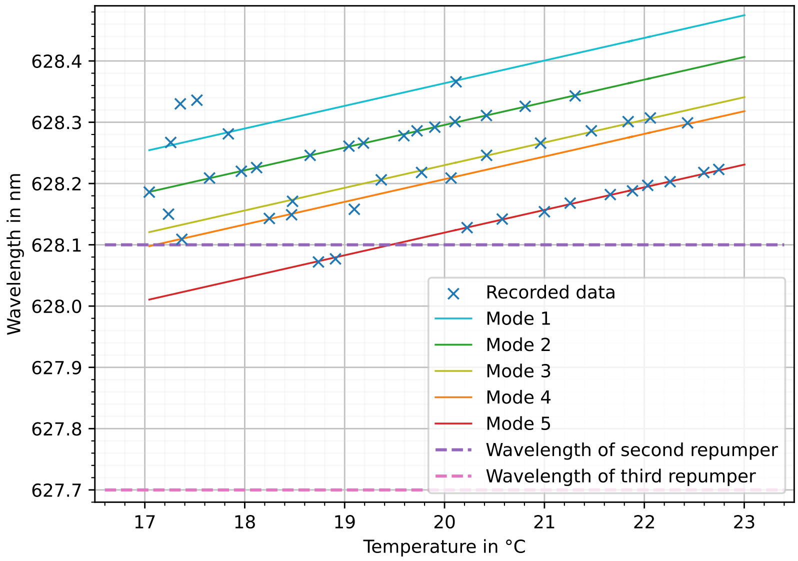

Figure 22: Wavelength of the second repump laser as a function of the diode temperature for a constant current of $I = 85.0\,\mathrm{mA}$. Different modes are shown as parallel lines with a gradient of $0.037\,\mathrm{nm}/°\mathrm{C}$. The plot also shows the wavelengths of the second and third repump transitions. It shows that it is possible to achieve the required wavelength for the second repump transition but not for the third.

longer intervals of the current before jumping into another mode.
The wavelength as a function of the temperature is shown in figure 22 for a constant diode current of $I = 85.0\,\mathrm{mA}$. The wavelength also increases linearly with increasing temperature or decreasing NTC resistance. Five different modes are indicated by parallel lines in the plot, which have a gradient of $0.037\,\mathrm{nm}/°\mathrm{C}$.
When increasing the temperature further, the laser suddenly jumps to higher wavelengths. For $T \geq 23.8\,°\mathrm{C}$, only wavelengths between $631.044\,\mathrm{nm}$ and $631.188\,\mathrm{nm}$ can be measured. As these are too far away from the target wavelength of $628.1\,\mathrm{nm}$, they are not shown in figure 22.
Both measurements show that it is possible to reach the wavelength of the second repump transition with this laser. However, it does not seem possible to reach the wavelength of $627.7\,\mathrm{nm}$ for a possible third repump transition. The current cannot be lowered further since the diode stops lasing when the current falls below the lasing threshold of $I = 62.8\,\mathrm{mA}$. It also becomes difficult to operate the laser at lower temperatures, since water from the air can condense and lead to an electrical short. Thus, a vacuum chamber would be required when lowering the temperature below approximately $14\,°\mathrm{C}$.

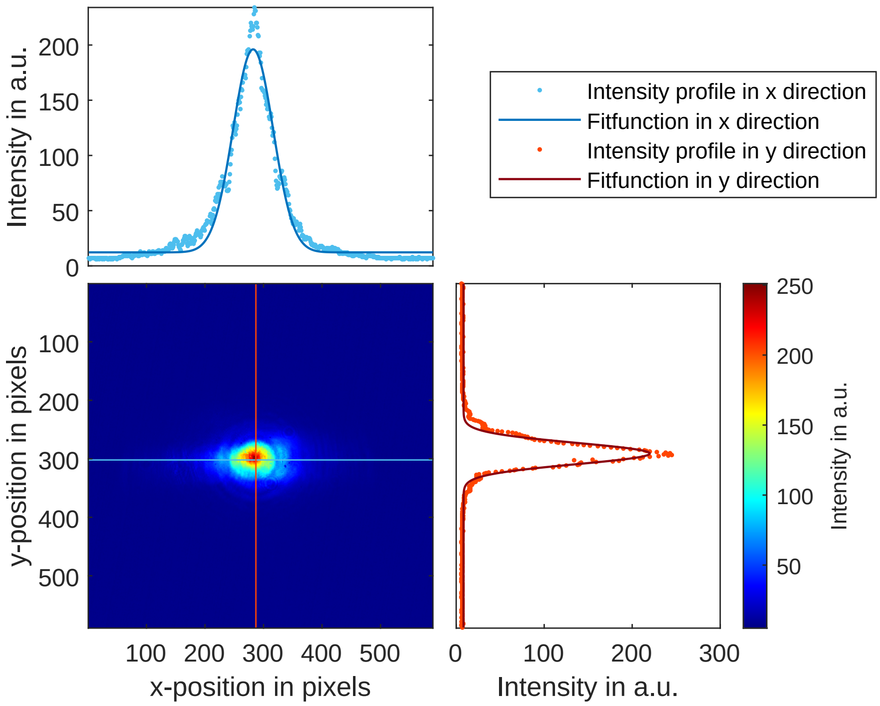

Figure 23: Beam profile of the second repump laser recorded directly behind the optical isolator. Intensity profiles through the center along the x- and y-direction are fitted with a Gaussian function to determine the beam diameters $d_x = 0.752\,\mathrm{mm}$ and $d_y = 0.401\,\mathrm{mm}$.

4.1.4 Beam Profile

Figure 23 shows the profile of the laser beam recorded directly behind the optical isolator. As it is typical for diode lasers, the beam profile is not perfectly round but elliptic. The major axis of the ellipse is tilted by approximately 10° to the horizontal and was corrected for the evaluation shown here. As a first step, a profile in x-direction is calculated as the sum of all elements in the respecting columns of the image. A profile in the y-direction is calculated as the sum of all elements in one line. In order to determine the center of the beam, these two profiles are fitted with a Gaussian function

$$f(x) = a \cdot \exp\left[-\frac{1}{2}\left(\frac{x-b}{c}\right)^2\right] \tag{4.2}$$

with the free parameters a, b and c. In addition to the recorded beam profile itself, figure 23 also shows the intensity profile along a horizontal and vertical line through the calculated beam center. These are fitted with the same Gaussian

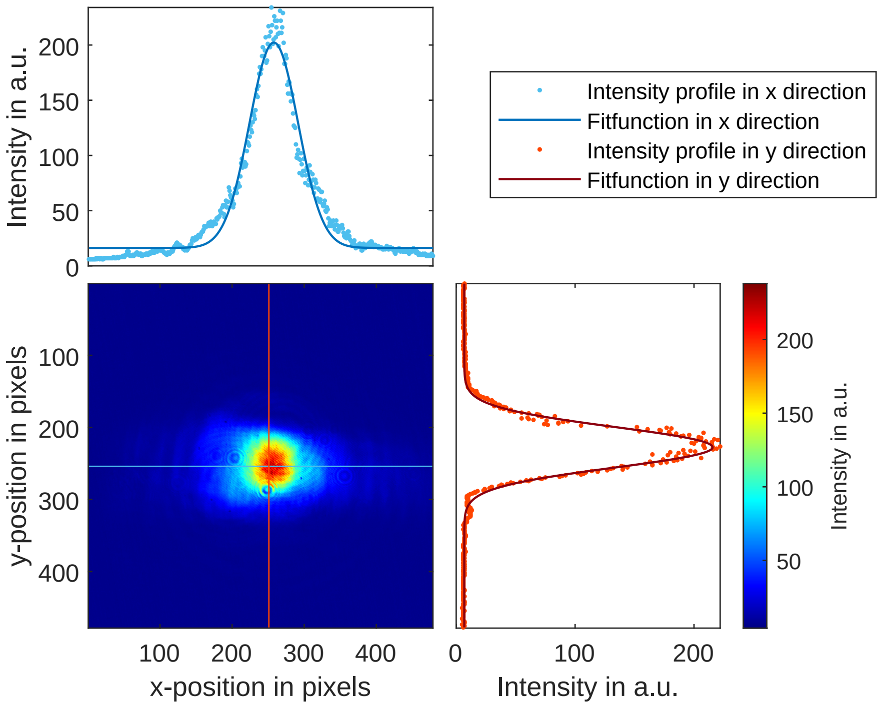

Figure 24: Beam profile of the second repump laser recorded directly before the fiber coupler leading to the EOM. Intensity profiles through the center along the x- and y-direction are fitted with a Gaussian function to determine the beam diameters $d_x = 0.743\,\mathrm{mm}$ and $d_y = 0.619\,\mathrm{mm}$.

function in (4.2). Each recorded pixel of the camera has a width and height of $5.5\,\mu\mathrm{m}$. This yields the beam diameters of $d_x = 0.752\,\mathrm{mm}$ in horizontal x-direction and $d_y = 0.401\,\mathrm{mm}$ in vertical y-direction.
Such an ellipticity can usually be corrected by letting the beam propagate through an anamorphic prism pair that scales the beam with a certain factor along the horizontal axis. This is done because only the part corresponding to a Gaussian beam can be coupled into the optical fiber. However, it turned out that the beam shows a very round profile directly before the fiber couplers even without any correction. The beam profile recorded before the fiber coupler leading to the EOM can be seen in figure 24 with the beam diameters of $d_x = 0.743\,\mathrm{mm}$ and $d_y = 0.619\,\mathrm{mm}$. Since this laser can be coupled into a fiber with high efficiency, a correction of the beam profile is not necessary.

4.2 Transfer Cavities for Frequency Locking

4.2.1 Spectra of the Cavities

The frequency of diode lasers needs to be stabilized since their wavelength can drift over time. Thus, we use a scanning transfer cavity lock for frequency locking of the slowing laser with $\lambda = 531.0\,\mathrm{nm}$, the cooling laser with $\lambda = 606.3\,\mathrm{nm}$, the first repump laser with $\lambda = 628.6\,\mathrm{nm}$ and the second repump laser with $\lambda = 628.1\,\mathrm{nm}$. Two of those lasers can each be coupled into one of the plano-concave cavities respectively together with the helium-neon laser as a reference. In this setup, only the beams of the second repump laser and the helium-neon laser are overlapped and coupled into cavity 1. Analogous to this, the first repump laser and the helium-neon laser are coupled into cavity 2. The helium neon laser operates at a wavelengh of $\lambda = 632.8\,\mathrm{nm}$ with a stability of $\pm 2.5\,\mathrm{MHz}$ over 24 hours.
The photodiode behind the second cavity mirror is connected to an oscilloscope to record the transmission curve. With only one laser coupled into the cavity, this is a periodic pattern of peaks, where the periodicity of the pattern is the FSR of the cavity and corresponds to the distance of peaks with the same height in this measurement. These are different longitudinal modes of the cavity where one more node of the incoming wave fits inside the cavity when increasing its length.
Peaks with different height correspond to different transversal modes of the laser beam. Those resulting from the TEM_{00} or Gaussian mode can be identified because the radial extent of different transversal modes increases with increasing order (l, m) of the modes as described in section 2.3.3. The peaks of higher modes can be suppressed in the transmission signal by closing the aperture at the second cavity mirror. If the cavity is well aligned with respect to the incoming beam, the fundamental Gaussian mode will be rather unaffected by this. The different transversal modes can also be observed by placing a screen behind the cavity instead of the photodiode. Some of the recorded modes can be seen in figure 25.
As the higher transversal modes are not rotationally symmetric, they are only observed if the cavity mirrors are sightly misaligned. Thus, the alignment of both cavity mirrors or of both mirrors in the laser's beam path can be optimized so that the transmitted intensity signal only shows the peaks of the Gaussian mode or at least the higher mode peaks are very small. This optimization is done individually for all lasers coupled into the cavity. The resulting transmission peaks can be seen in figure 26 for cavity 1.
The whole pattern of peaks can be shifted along the x-axis with an offset in the piezo voltage. But this can also occur due to changes in temperature or air pressure. The relative distance between the respective peaks of the different lasers is kept constant by the laser locking scheme.

(a) TEM_{00} mode (b) TEM_{10} mode (c) TEM_{20} mode (d) TEM_{30} mode (e) TEM_{40} mode

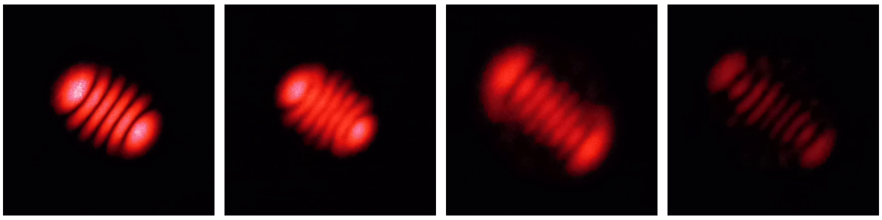

(f) TEM_{50} mode (g) TEM_{60} mode (h) TEM_{70} mode (i) TEM_{80} mode

Figure 25: Different transversal modes of the helium-neon laser visible as transmitted light of cavity 2 before improving the alignment of the cavity mirrors. The images are recorded for a piezo ramp frequency of only $\nu = 20\,\mathrm{mHz}$ to distinguish the different modes.

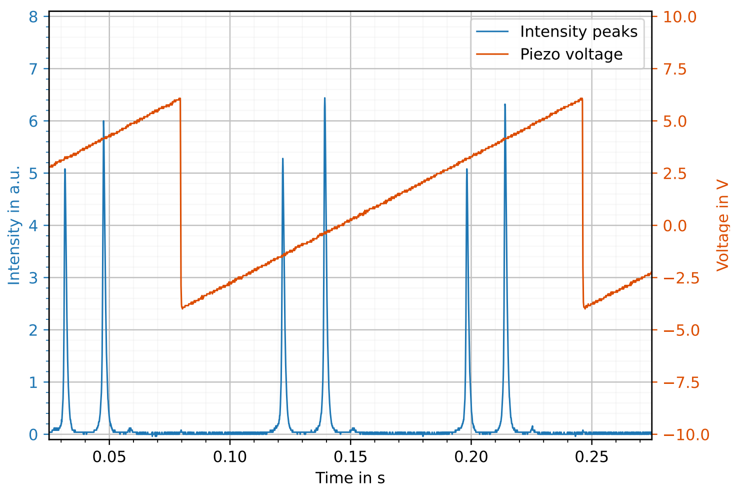

Figure 26: Transmitted intensity peaks of the second repump laser and the helium-neon laser observed on cavity 1. The voltage applied to the piezo at the plane mirror is a ramp voltage with frequency $\nu = 6\,\mathrm{Hz}$ and amplitude $V_{\mathrm{pp}} = 10\,\mathrm{V}$. The cavity mirrors are aligned so that no higher laser modes are recorded.

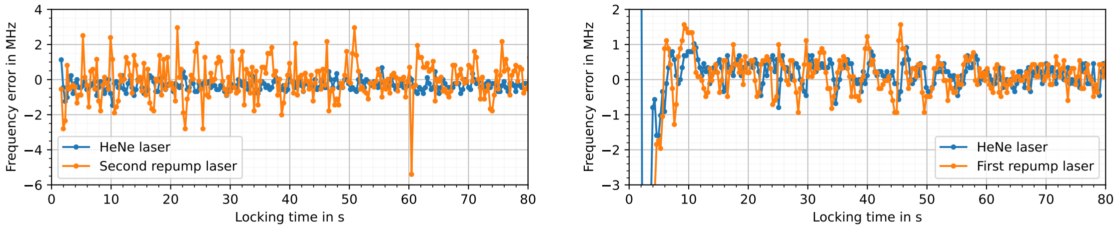

(a) Cavity 1

(b) Cavity 2

Figure 27: Error signals of the helium-neon laser and the respective repump laser on both cavities during the laser locking. These signals are used as a feedback to stabilize the cavity by applying an offset to the piezo voltage and to stabilize the repump laser frequency by adjusting the diode current.

4.2.2 Frequency Locking

Fluctuations of the cavity shift the peaks of all lasers the same. Thus, also the reference laser drifts from its initial position on the scan. The deviation of the helium-neon laser peak from its intended peak position is calculated as an error signal. This is used as a feedback for the locking program. The cavity is stabilized by giving an offset to the triangular scan voltage applied to the piezo. This keeps the reference laser peak at a constant position as long as the cavity does not drift too far and the drift can still be compensated by the offset voltage.

Fluctuations of the frequencies of both repump lasers also affect their peak position, which is recorded as an error signal. The frequency lock stabilizes their distance to the reference peak by varying the diode current of the lasers [26].

Figure 27 shows the errors signals of the helium-neon laser and the respective repump laser during the locking. The error due to the cavity drift stays in the range of $\pm 2\,\text{MHz}$ for both cavities. The errors have a standard deviation of $\sigma_{\text{c1}} = 0.356\,\text{MHz}$ and $\sigma_{\text{c2}} = 0.318\,\text{MHz}$ which are similar for both cavities. The first repump laser, which is a commercial design, is comparably stable with a standard deviation of $\sigma_{\text{r1}} = 0.412\,\text{MHz}$. Its error is also kept in a range of $\pm 2\,\text{MHz}$ with only two higher fluctuations of $-2.19\,\text{MHz}$ and $-2.76\,\text{MHz}$ over a locking time of $477\,\text{s}$. However, the second repup laser shows higher errors with a standard deviation of $\sigma_{\text{r2}} = 1.077\,\text{MHz}$ and is less stable.

These errors are small enough compared to the natural linewidth of the A-X transition which is $8.3\,\text{MHz}$ [20]. To improve the stability further, both cavities can also be protected from external influences by a casing.

4.2.3 Linewidth

The width of the transmitted intensity peaks is also determined from the measurement displayed in figure 26. The peak caused by the diode laser has a full width at half maximum of $\Delta\nu_{\mathrm{DL}} = 14.583\,\mathrm{MHz}$ and the peak of the helium-neon laser has a width of $\Delta\nu_{\mathrm{HeNe}} = 13.949\,\mathrm{MHz}$. The frequency resolution calculated for both cavities is $\Delta\nu = 4.331\,\mathrm{MHz}$, which is smaller than the recorded peak widths. However, both peak widths are too large to be caused only by the laser linewidth of a helium-neon or a diode laser. Therefore, the cavity resolution is probably not as good as calculated above. The cavity mirrors might not be aligned perfectly or the resonator length L could be a little smaller than 15 cm, which would increase the peak width.

4.3 Electro-Optical Modulation of the Second Repump Laser

To account for the hyperfine splitting of the ground state of CaF that is shown in figure 5(b), the second repump laser needs to be modulated. This is done with an electro-optical modulator. The following section details the characterization of the phase modulation setup.

4.3.1 Modulation with a Sinusoidal Signal

The phase modulator is first characterized by applying a sinusoidal voltage. The light beam from the second repump laser is directly coupled into the input fiber of the modulator. The output fiber is then connected to the fiber leading to cavity 1 via a fiber-to-fiber connector. The output fiber of the EOM is not connected directly to the outcoupler because the EOM's output and input fibers have a different mode field diameter than the fibers used in the rest of the setup. This would lead to a different beam diameter that cannot be focused correctly by the coupling lens with given focal length. Only a little more than half the power is transmitted through the fiber-to-fiber connection, which is sufficient to record the transmission peaks of the cavity on an oscilloscope.
For a diode current of $I = 86.00\,\mathrm{mA}$ the transmission of the cavity shows clear frequency peaks. As they fluctuate a little in height and along the x-axis, the signal is averaged over a few seconds before recording the data. Thus, the frequency peaks get a little broader.
The sinusoidal signal applied to the EOM is generated by an arbitrary waveform

generator[12]. The waveform set at the AWG is a sine with 50 oscillations per cycle, which corresponds to a frequency of $\nu = 50\,\mathrm{MHz}$. The lowest value that can be set for the amplitude of the AWG output voltage is $20\,\mathrm{mV}$. Therefore, a first measurement is recorded for $V = 0\,\mathrm{mV}$ and the output voltage is then increased from $V = 20\,\mathrm{mV}$ to $200\,\mathrm{mV}$ in steps of $10\,\mathrm{mV}$. This output voltage is also amplified to $\tilde{V}_{\mathrm{pp}}$ by an amplifier[13] with a voltage gain of $29\,\mathrm{dB}$.
The transmitted intensity peaks are recorded for each amplitude and can be seen in figure 28(a) from the bottom up for increasing modulation voltage. Since the position of the peaks on the oscilloscope with respect to the piezo ramp voltage drifts over time, all recorded peak patterns are corrected by a specific offset on the x-axis so that all carrier frequency peaks are vertical to each other.
In the measurement for an amplitude of $V = 80\,\mathrm{mV}$, the group of peaks is recorded twice during one voltage ramp. Therefore, this measurement is used to determine the distance of the carrier frequency peaks $t_{\mathrm{FSR}} \approx 77\,\mathrm{ms}$, which corresponds to the free spectral range on the time axis. Since

$$\frac{\Delta t}{t_{\mathrm{FSR}}} = \frac{\Delta \nu}{\nu_{\mathrm{FSR}}}, \tag{4.3}$$

the time axis of the oscilloscope is re-scaled to show the frequency shift of the generated sidebands with respect to the carrier frequency. Figure 28(a) shows that the sidebands are created with shifts of approximately an integer multiple of $50\,\mathrm{MHz}$ as expected from equation (2.37). For example with the modulation voltage amplitude of $V = 80\,\mathrm{mV}$, the first order sidebands have a frequency distance of $\Delta\nu_1 = 53.247\,\mathrm{MHz}$ to the carrier frequency and the second order sidebands have a distance of $\Delta\nu_2 = 106.493\,\mathrm{MHz}$. This result differs only slightly from the expected frequencies of $50\,\mathrm{MHz}$ and $100\,\mathrm{MHz}$.
Additionally, the heights of all frequency peaks are determined by finding the maximum in the respective intervals that are indicated by dotted lines in the plot. The peak heights of the carrier frequency and all the visible sidebands from order 1 to 3 as a function of the output voltage are shown in figure 28(b). Without a voltage applied to the phase modulator, the carrier frequency has its maximum height and no sidebands are created. When increasing the modulation voltage, power is transferred from the carrier frequency to the sidebands. Therefore, the height of the carrier frequency peak decreases while the first order sidebands become higher and even more sidebands appear for increasing voltage.
According to equation (2.37), the heights of the sideband peaks with order l are described by the squared Bessel functions J_l^2. Thus, the heights of the carrier

[12]Tektronix AWG2041
[13]Mini-Circuits ZH-1-2W+

frequency are fitted with the function

$$f(V) = a \cdot J_0 (bV)^2 . \tag{4.4}$$

with the free parameters $a = 5.680$ in the arbitrary units of the intensity and $b = 17.692\,\mathrm{V}^{-1}$. The higher order functions are also plotted for the same parameters.

The Bessel function that describes the height of the carrier frequency peaks becomes zero for $bV = 2.4$ and therefore $V_{\mathrm{min}} = 135.66\,\mathrm{mV}$. Since this voltage is amplified with 29 dB, the corresponding voltage applied to the phase modulator is

$$\tilde{V}_{\mathrm{pp,min}} = 135.66\,\mathrm{mV} \cdot 2 \cdot 10^{\frac{29}{20}} \approx 7.647\,\mathrm{V}.$$

The modulation depth is

$$\beta = \frac{\phi_0}{\pi} = \frac{\tilde{V}_{\mathrm{pp}}}{2V_\pi}$$

and the peak height is also described by $J_0(\phi_0)^2$. Thus, the half wave voltage

$$V_\pi = \frac{\pi \tilde{V}_{\mathrm{pp}}}{2\phi_0} = \frac{\pi \cdot 7.647\,\mathrm{V}}{2 \cdot 2.4} \approx 5.005\,\mathrm{V}$$

can be calculated. This agrees well with the datasheet of the phase modulator, which lists a typical half wave voltage of $V_\pi = 5\,\mathrm{V}$.

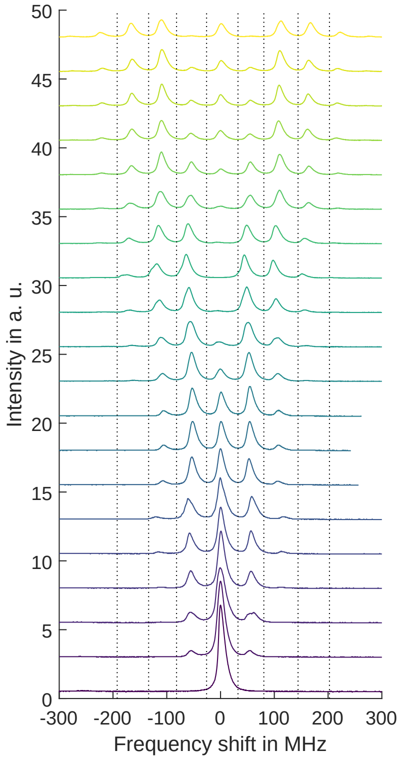

(a)

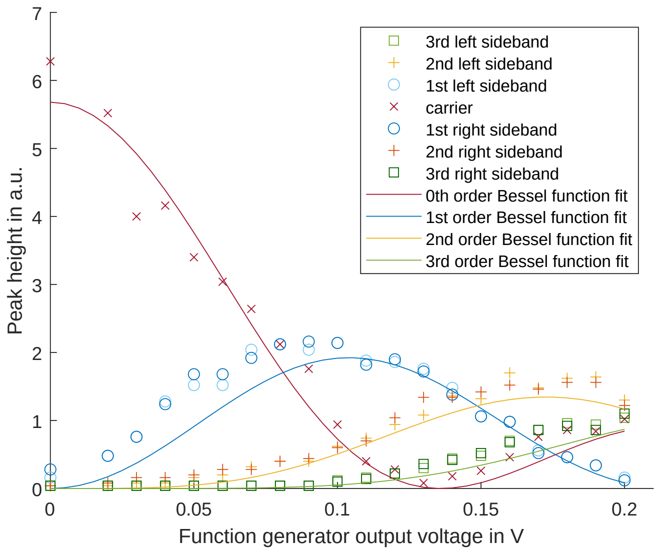

(b)

Figure 28: (a) Transmitted intensity peaks at cavity 1 for the phase modulated light of the second repump laser. The peaks are recorded for function generator amplitudes of 0 mV and 20 mV to 200 mV in steps of 10 mV and shown from the bottom up for increasing modulation voltage. As expected for sinusoidal modulation, the sidebands are created at frequency distances of approximately an integer multiple of the frequency 50 MHz of the applied voltage. (b) The frequency peak heights of the carrier frequency and all the visible sidebands from order 1 to 3 as a function of the AWG output voltage. The heights are fitted with a Bessel function for the carrier frequency peak to calculate the half wave voltage of $V_\pi = 5.005\,\mathrm{V}$.

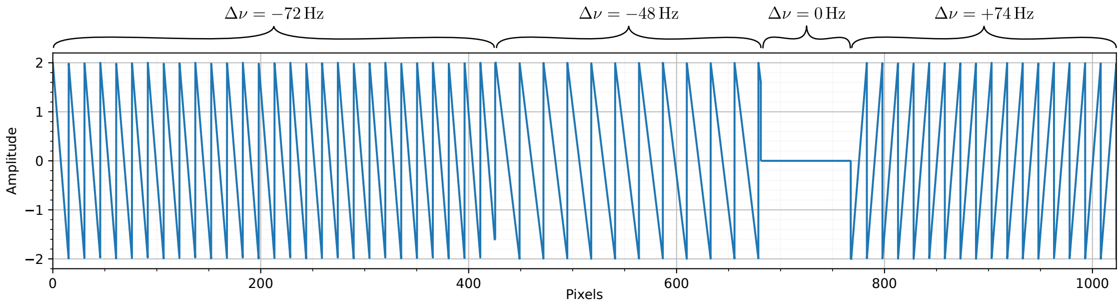

Figure 29: Serrodyne signal applied to the phase modulator in order to create sidebands to address the hyperfine levels of the ground state in CaF molecules. The gradient of the ramps in the first, second and fourth interval leads to frequency shifts of $-72\,\mathrm{MHz}$, $-48\,\mathrm{MHz}$ and $74\,\mathrm{MHz}$. The third interval does not cause a frequency shift.

4.3.2 Modulation with a Serrodyne Signal

To create a spectrum of frequencies that cover the hyperfine splitting of the ground state in CaF molecules as shown in figure 5(b), a serrodyne signal produced by the AWG is applied to the phase modulator.

Since the ground state splits into four hyperfine levels, the required spectrum consists of the four corresponding frequency peaks shifted by $+74\,\mathrm{MHz}$, $0\,\mathrm{MHz}$, $-48\,\mathrm{MHz}$ and $-72\,\mathrm{MHz}$ with respect to the carrier frequency. The serrodyne signal therefore consists of four intervals with different length and a different number of ramp oscillations. The ramps with different gradients each lead to a different frequency shift $\Delta\nu$. Since the total signal is repeated with a clock frequency of $1.024\,\mathrm{GHz}$, all four frequency peaks can be observed at the same time.

Additionally, the four hyperfine levels differ in their total angular momentum quantum number F and have each $2F+1$ sublevels with the same energy. The frequency shifted by $-72\,\mathrm{MHz}$ addresses an energy level with $F = 2$ including five sublevels whereas the carrier frequency addresses an energy with $F = 0$ without additional sublevels. Therefore, the frequency peak shifted by $-72\,\mathrm{MHz}$ needs to be five times as high as the carrier frequency peak. Analogous, the peaks shifted by $-48\,\mathrm{MHz}$ and $74\,\mathrm{MHz}$ need to be three times as high as the carrier frequency peak. This is realized by choosing the interval lengths approximately in the ratio 5:3:1:3.

The applied serrodyne signal is shown in figure 29. The interval length in pixels, the number of oscillations and the amplitude set for each interval at the AWG are listed in table 1.

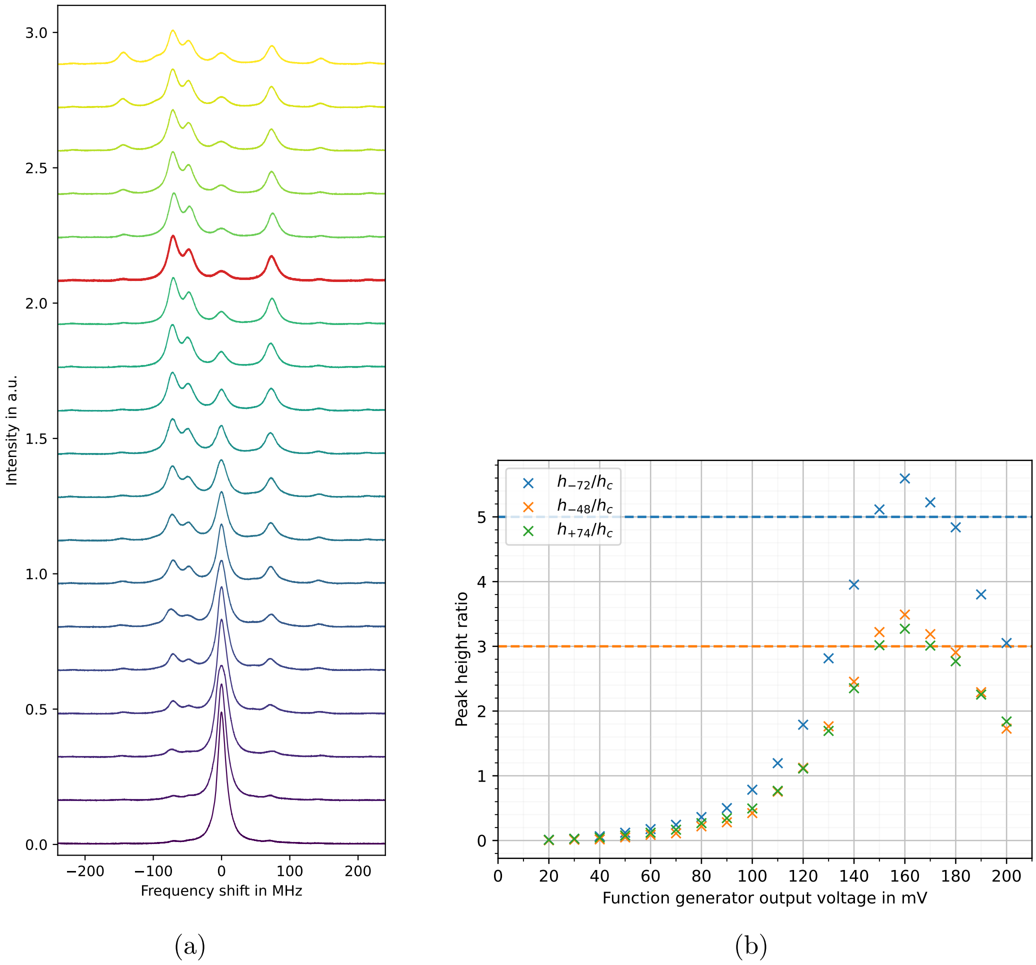

Figure 30: (a) Transmitted intensity peaks at cavity 1 for the phase modulated light of the second repump laser. The peaks are recorded for function generator amplitudes of 0 mV and 20 mV to 200 mV in steps of 10 mV and shown from the bottom up for increasing modulation voltage. The sidebands are approximately created at the intended frequency distances of +74 MHz, −48 MHz and −72 MHz to the carrier frequency. The peak pattern that fulfills the required frequency distances and peak height ratios the best is highlighted in red. (b) Height ratios of the shifted frequency peaks to the carrier frequency peak calculated as a function of the voltage amplitude. The required ratios of $h_{\text{-}72}/h_\mathrm{c} = 5$ and $h_{\text{-}48}/h_\mathrm{c} = h_{+74}/h_\mathrm{c} = 3$ are also shown. For a voltage of $V = 150\,\mathrm{mV}$ the ratios come closest to the targets.

Table 1: Settings of the AWG to produce the serrodyne signal.

Pixels	Number of oscillations	Amplitude
0 ... 425	27.9	-2
426 ... 681	11.1	-2
682 ... 767	0	0
768 ... 1023	17.0	2

The resulting intensity peaks transmitted at cavity 1 are shown in figure 30(a) from the bottom up for increasing voltage amplitudes. Analogous to the measurement in the previous section, the amplitude is first set to $V = 0\,\mathrm{mV}$ and then increased from $20\,\mathrm{mV}$ to $200\,\mathrm{mV}$ in steps of $10\,\mathrm{mV}$.
A single transmission peak of the cavity can be described by a Lorentz function

$$L(\Delta\nu, a, b, c) = \frac{a}{1 + b(\Delta\nu - c)^2} \tag{4.5}$$

with the free parameters a, b and c. To determine the peak positions and heights for all voltage amplitudes, the recorded curves are fitted with the function

$$f(\Delta\nu) = L_1 + L_2 + L_3 + L_4 + d \tag{4.6}$$

which is the sum of four Lorentz functions with a total of twelve parameters and a constant offset d. This evaluation yields that the frequency shifts of the peaks are approximately constant for increasing voltage amplitude.
The peak heights $h_{\text{-}72}$, $h_{\text{-}48}$, h_{c} and h_{+74} are also calculated as a function of the voltage amplitude. The ratios of the heights of the shifted frequency peaks to the carrier frequency peak as well as the required ratios of $h_{\text{-}72}/h_{\mathrm{c}} = 5$ and $h_{\text{-}48}/h_{\mathrm{c}} = h_{+74}/h_{\mathrm{c}} = 3$ are shown in figure 30(b). The plot shows that the height ratios come closest to the target for a voltage of $V = 150\,\mathrm{mV}$. For higher voltages, more power is transferred into higher order peaks that appear for an integer multiple of the required frequencies.
The recorded peak curve for $150\,\mathrm{mV}$ is highlighted in figure 30(a) and shown with the fitted function in figure 31. Figure 32 shows, in addition to the recorded peaks, the individual Lorentz functions that make up the total fitfunction without the constant offset. For frequency peaks that are positioned close to each other the peak heights of the individual Lorentz functions clearly differ from the heights of their sum and also the positions are shifted slightly with respect to the total fitfunction. This is due to the limited resolution of the cavity that determines the peak width in addition to the linewidth of the laser itself. The figure also shows the required transition frequencies as inverted peaks with a width of $8.3\,\mathrm{MHz}$. This corresponds to the natural linewidth of the A-X transition [20]. The peak positions

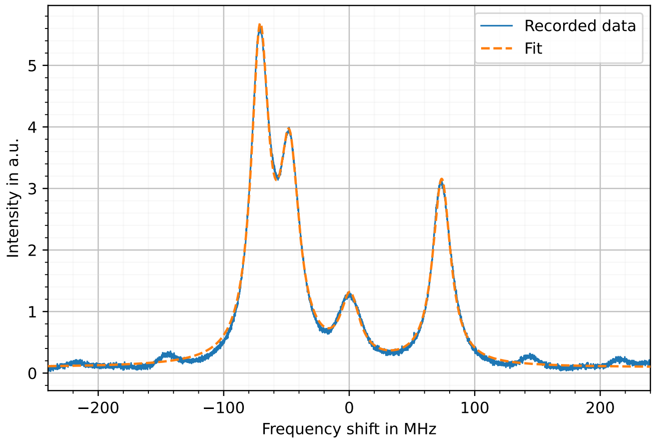

Figure 31: Transmitted intensity peaks at cavity 1 for the phase modulated light of the second repump laser for a function generator amplitude of $V = 150\,\mathrm{mV}$. The data is fitted with the sum of four Lorentz functions which shows that this spectrum fulfills the requirements for the frequency shifts and peak height ratios the best.

$\Delta\nu$ with respect to the carrier frequency and the height ratios for the amplitude of $150\,\mathrm{mV}$ that are a result of the fitted function are listed in table 2. It shows that the sidebands created by phase modulation agree well with the theoretically required peaks. The frequency shift $\Delta\nu_{+74}$ has the largest deviation from theory of $\approx 1\,\mathrm{MHz}$. But compared to the linewidth of $8.3\,\mathrm{MHz}$, this still agrees well with the expected values.

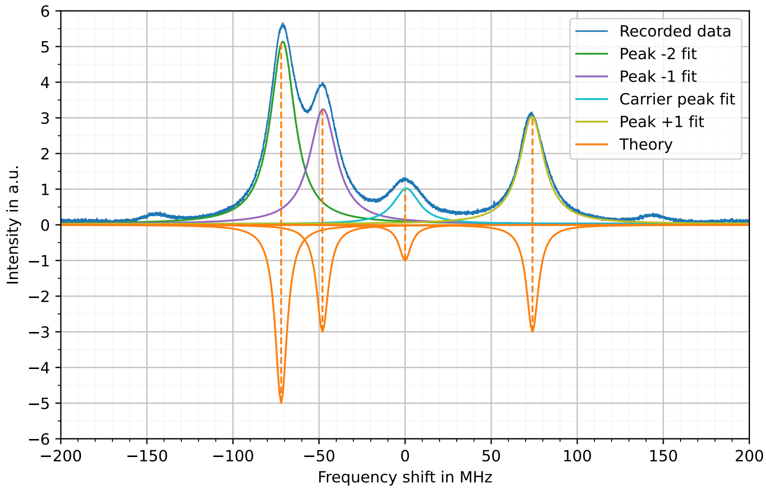

Figure 32: Transmitted intensity peaks at cavity 1 for the phase modulated light of the second repump laser for a function generator amplitude of $V = 150\,\mathrm{mV}$. The plot also shows the individual Lorentz functions that make up the total fitfunction without the constant offset. For comparison, the required transition frequencies are shown as inverted peaks with a width of 8.3 MHz. This shows that the sidebands created by phase modulation agree well with the theoretically required peaks.

Table 2: Positions with respect to the carrier frequency and height ratios of the frequency sidebands created by phase modulation. The theoretical values are listed for comparison. This shows that the created frequency spectrum agrees well with the theory since all deviations from theory are small compared to the natural linewidth of 8.3 MHz.

	Recorded for $V = 150\,\mathrm{mV}$	Theory
$\Delta\nu_{-72}$	$-71.780\,\mathrm{MHz}$	$-72\,\mathrm{MHz}$
$\Delta\nu_{-48}$	$-48.383\,\mathrm{MHz}$	$-48\,\mathrm{MHz}$
$\Delta\nu_{+74}$	$72.969\,\mathrm{MHz}$	$74\,\mathrm{MHz}$
h_{-72}/h_{c}	5.115	5
h_{-48}/h_{c}	3.220	3
h_{+74}/h_{c}	3.017	3

5 Summary and Outlook

In this thesis, the second repumper on the X-A transition for the laser cooling of calcium monofluoride molecules has been set up and characterized. The beam profile of this laser is good enough to be coupled into a fiber with a high efficiency without requiring a prism pair to correct the ellipticity. With the selected laser diode, the laser can achieve the required wavelength without being cooled to temperatures that would require a vacuum chamber. It can emit up to 52 mW, but for a wavelength of $\lambda = 628.1$ nm only a power of approximately 20 mW can be achieved. Therefore, it will have to be tested how much power is required for the frequency locking and the wavemeter and if the remaining fraction is sufficient for the experiment. The experiment will require approximately 10 mW [17]. However, if it turns out that the power is decreased too strongly by the optical components and fibers and is not sufficient for the experiment, the setup can be extended to a leader-follower setup. This consists of a frequency locked laser with low power, which provides feedback to another laser diode with higher power that then emits at the same wavelength. Such a setup could be adapted with a second identical laser diode.

Moreover, the laser was frequency locked with a scanning transfer cavity for a short time, during which the laser frequency fluctuates approximately by ± 3 MHz with a standard deviation of $\sigma_{r2} = 1.077$ MHz. The second repump laser is not as stable as the first repump laser, which is a commercial laser, but this is nonetheless sufficient for a laser on the X-A transition of CaF, as the natural linewidth of the transition is 8.3 MHz. The laser will eventually be required to remain locked for hours at a time. Therefore, it will also be necessary to confirm that the lock remains stable over long periods of time. To further stabilize the cavities, they can be encased in order to protect them from external influences. The setup can also be extended to couple the slowing and cooling laser into the cavities and lock them analogous to the other two lasers.

Finally, the fiber EOM which generates the sidebands to address the hyperfine splitting of the ground state in CaF was characterized. Applying a sinusoidal voltage to the EOM generates symmetrical sidebands at integer multiples of the modulation frequency in the spectrum. With these, the half-wave voltage of $V_\pi \approx 5$ V was determined. The required frequency spectrum of the A-X transition was generated by applying a sequence of serrodyne signals to the fiber EOM. For a function generator output voltage of $V = 150$ mV the spectrum features sidebands with frequency shifts of 74 MHz, 0 MHz, -48 MHz and -72 MHz with the intensity ratios 3, 1, 3 and 5 as required.

Together with the slowing laser, cooling laser and the first repump laser the second repump laser completes the lineup of lasers that are necessary for the laser cooling of CaF. The next experimental steps involve the first pumpdown and cooldown to cryogenic temperatures of the source chamber which contains the buffer gas beam source. When the first molecules have been produced and detected, the beam source will have to be characterized. Once a reliable molecular beam can be produced, the lasers will be used for transversal cooling and longitudinal slowing of the molecular beam as well as magneto-optical trapping of a slowed molecular cloud.

6 Appendix

6.1 Thermistor Characteristics

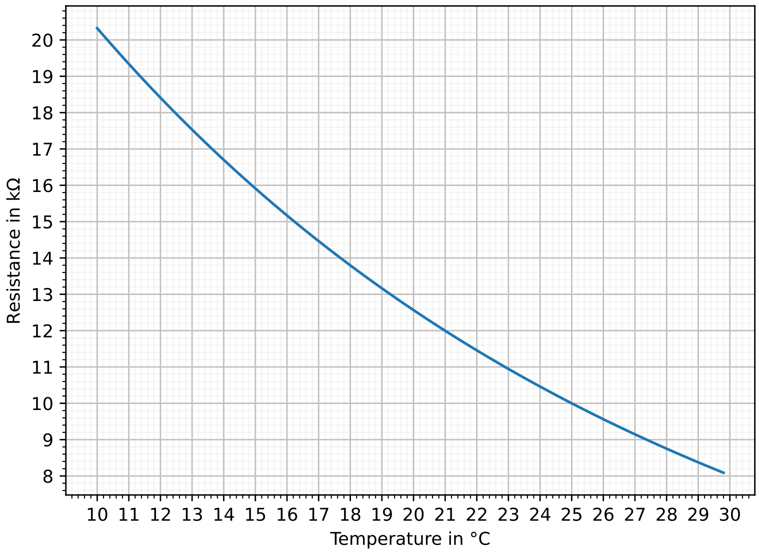

Figure 33: Thermistor resistance as a function of temperature. This curve is used to calculate the laser diode temperature from the thermistor resistance recorded by the temperature controller of the second repump laser.

The thermistor connected to the temperature controller of the second repump laser is a RS 151-237 NTC. Its resistance R at any temperature T in Kelvin that is within the operating range can be calculated with

$$R(T) = R_0 \cdot \exp\left(\frac{B}{T} - \frac{B}{T_0}\right) \tag{6.1}$$

where $R_0 = 10\,\mathrm{k\Omega}$ is the thermistor resistance at the temperature $T_0 = 25\,°\mathrm{C}$. The characteristic temperature constant $B = 3991.448\,\mathrm{K}$ is derived from the thermistor resistance at 25 °C and 100 °C [32]. The temperature can be calculated from the recorded thermistor resistance by solving equation (6.1) for T.

6.2 Reflectivity of the Cavity Mirrors

The transmitted intensity peaks of both cavities have a width that is higher than expected from the resolution $\Delta\nu$ for the mirror reflectivity $\tilde{R} = 99.5\,\%$ listed in the datasheet. Therefore, the reflectivity of both mirrors was measured as a function of the wavelength at the 4th Institute of Physics. These measurements were recorded for an incidence angle close to zero and are depicted in figure 34 for the plane mirror and in figure 35 for the curved mirror. The reflectivity for a wavelength of 628 nm is $\tilde{R}_\mathrm{p} = 98.901\,\%$ for the plane mirror and $\tilde{R}_\mathrm{c} = 98.397\,\%$ for the curved mirror. These values are calculated as the mean value of the reflectivity for s-polarized and p-polarized light.

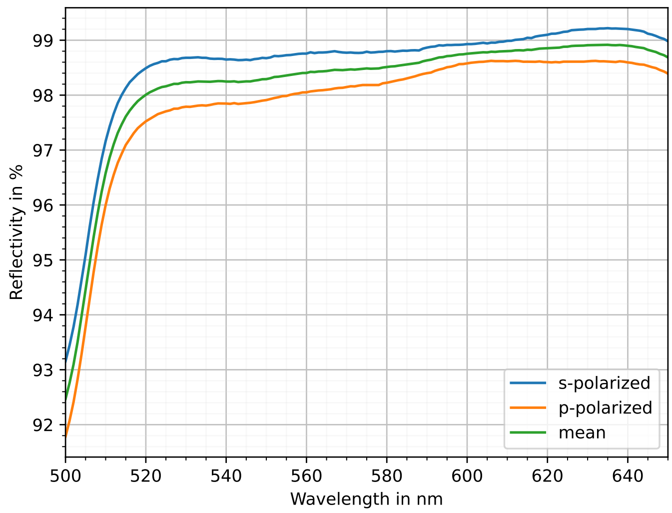

Figure 34: Reflectivity of the plane cavity mirror as a function of the wavelength for s-polarized and p-polarized light as well as the mean value of both.

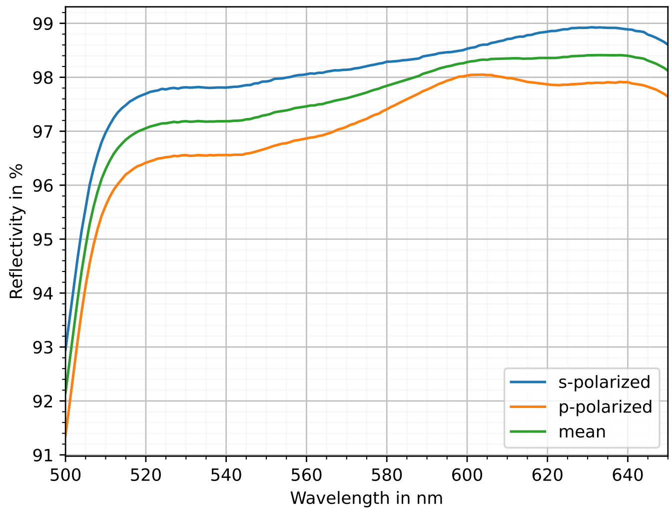

Figure 35: Reflectivity of the curved cavity mirror as a function of the wavelength for s-polarized and p-polarized light as well as the mean value of both.

7 References

[1] T. W. Hänsch and A. L. Schawlow. "Cooling of gases by laser radiation". In: *Optics Communications* 13.1, (68–69) (1975). URL: `https://doi.org/10.1016/0030-4018(75)90159-5`.

[2] M. R. Tarbutt. "Laser Cooling of Molecules". In: *Contemporary Physics* 59.4, (356-376) (2018). URL: `https://doi.org/10.1080/00107514.2018.1576338`.

[3] D. J. Wineland, R. E. Drullinger, and F. L. Walls. "Radiation-Pressure Cooling of Bound Resonant Absorbers". In: *Physical Review Letters* 40, (1639) (1978). URL: `https://doi.org/10.1103/PhysRevLett.40.1639`.

[4] S. Chu, L. Hollberg, J. E. Bjorkholm, A. Cable, and A. Ashkin. "Three-dimensional viscous confinement and cooling of atoms by resonance radiation pressure". In: *Physical Review Letters* 55, (48) (1985). URL: `https://doi.org/10.1103/PhysRevLett.55.48`.

[5] T. Rosenband, D. B. Hume, P. O. Schmidt, et al. "Frequency Ratio of Al^+ and Hg^+ Single-Ion Optical Clocks; Metrology at the 17th Decimal Place". In: *Science* 319.5871, (1808-1812) (2008). URL: `https://doi.org/10.1126/science.1154622`.

[6] A. Micheli, G. Brennen, and P. Zoller. "A toolbox for lattice-spin models with polar molecules". In: *Nature Physics* 2, (341–347) (2006). URL: `https://doi.org/10.1038/nphys287`.

[7] J. Hudson, D. Kara, and I. Smallman. "Improved measurement of the shape of the electron". In: *Nature* 473, (493-496) (2011). URL: `https://doi.org/10.1038/nature10104`.

[8] S. Truppe, R. Hendricks, S. Tokunaga, et al. "A search for varying fundamental constants using hertz-level frequency measurements of cold CH molecules". In: *Nature Communications* 4, (2600) (2013). URL: `https://doi.org/10.1038/ncomms3600`.

[9] E. R. Hudson, H. J. Lewandowski, B. C. Sawyer, and J. Ye. "Cold Molecule Spectroscopy for Constraining the Evolution of the Fine Structure Constant". In: *Physical Review Letters* 96, (143004) (2006). URL: `https://doi.org/10.1103/PhysRevLett.96.143004`.

[10] L. W. Cheuk, L. Anderegg, Y. Bao, S. Burchesky, S. S. Yu, W. Ketterle, K. Ni, and J. M. Doyle. "Observation of Collisions between Two Ultracold

Ground-State CaF Molecules”. In: *Physical Review Letters* 125, (043401) (2020). URL: https://doi.org/10.1103/PhysRevLett.125.043401.

[11] Y. Liu, MG. Hu, M. A. Nichols, et al. “Photo-excitation of long-lived transient intermediates in ultracold reactions”. In: *Nature Physics* 16, (1132–1136) (2020). URL: https://doi.org/10.1038/s41567-020-0968-8.

[12] M. D. Di Rosa. “Laser-cooling molecules. Concept, candidates, and supporting hyperfine-resolved measurements of rotational lines in the A–X(0,0) band of CaH”. In: *European Physical Journal D* 31, (395–402) (2004). URL: https://doi.org/10.1140/epjd/e2004-00167-2.

[13] L. Anderegg. “Ultracold Molecules in Optical Arrays: From Laser Cooling to Molecular Collisions”. PhD thesis. Harvard University, 2019. URL: https://nrs.harvard.edu/URN-3:HUL.INSTREPOS:37365119.

[14] M. Schmidt, L. Lassablière, G. Quéméner, and T. Langen. “Self-bound dipolar droplets and supersolids in molecular Bose-Einstein condensates”. In: *Physical Review Research* 4, (013235) (2022). URL: https://doi.org/10.1103/PhysRevResearch.4.013235.

[15] I. Kozyryev, L. Baum, K. Matsuda, et al. “Sisyphus Laser Cooling of a Polyatomic Molecule“. In: *Physical Review Letters* 118, (173201) (2017). URL: https://doi.org/10.1103/PhysRevLett.118.173201.

[16] L. Baum, N. B. Vilas, C. Hallas, et al. “1D Magneto-Optical Trap of Polyatomic Molecules“. In: *Physical Review Letters* 124, (133201) (2020). URL: https://doi.org/10.1103/PhysRevLett.124.133201.

[17] H. J. Williams. “Producing, trapping and controlling ultracold CaF molecules”. PhD thesis. Imperial College London, 2018.

[18] H. Haken and H. C. Wolf. *Molekülphysik und Quantenchemie. Einführung in die experimentellen und theoretischen Grundlagen*. Springer, 2006. ISBN: 978-3-540-30314-5.

[19] H. J. Williams, S. Truppe, M. Hambach, et al. “Characteristics of a magneto-optical trap of molecules”. In: *New Journal of Physics* 19, (113035) (2017). URL: https://doi.org/10.1088/1367-2630/aa8e52.

[20] N. J. Fitch and M. R. Tarbutt. “Laser-cooling Molecules”. In: *Advances in Atomic, Molecular & Optical Physics* 70, (157-262) (2021). URL: https://doi.org/10.1016/bs.aamop.2021.04.003.

[21] C. E. Rogers, J. L. Carini, J. A. Pechkis, and P. L. Gould. "Creation of arbitrary time-sequenced line spectra with an electro-optic phase modulator". In: *Review of Scientific Instruments* 82, (073107) (2011). URL: `https://doi.org/10.1063/1.3611005`.

[22] W. Demtröder. *Experimentalphysik 3. Atome, Moleküle und Festkörper*. Springer, 2016. ISBN: 978-3-662-49094-5 (eBook).

[23] F. J. Duarte. *Tunable Lasers Handbook*. Academic Press, 1995. ISBN: 978-0-12-222695-3.

[24] Thorlabs Inc. *Diffraction Gratings Tutorial.* `https://www.thorlabs.com/newgrouppage9.cfm?objectgroup_id=9026`.

[25] B. E. A. Saleh and M. C. Teich. *Fundamentals of Photonics.* John Wiley & Sons, Inc., 2019. ISBN: 9781119506874.

[26] E. Pultinevicius, "A laser frequency stabilization scheme for the cooling of barium monofluoride molecules". Master's thesis. University of Stuttgart, 2022.

[27] W. Demtröder. *Experimentalphysik 2. Elektrizität und Optik.* Springer, 2017. ISBN: 978-3-662-55790-7 (eBook).

[28] D. Meschede. *Optik, Licht und Laser*. Vieweg + Teubner, 2008. ISBN: 987-3-8351-0143-2 (eBook).

[29] JENOPTIK Optical Systems GmbH. *Integrated-optical modulators. Technical information and instructions for use.* URL: `https://www.jenoptik.com/products/optoelectronic-systems/light-modulation/integrated-optical-modulators-fiber-coupled/phase-modulator`.

[30] Thorlabs Inc. *Fiber-Coupled Electro-Optic Modulator Lab Facts.* URL: `https://www.thorlabs.com/newgrouppage9.cfm?objectgroup_id=10833`.

[31] Toptica Photonics. *Laser Diode Data Sheet. Semiconductor Laser Diode LD-0633-0100-1.*

[32] RS Components. *Thermistors. Data Sheet.*

All links were last accessed on 22.02.2023.

Acknowledgments

I would like to thank the following people:

- Prof. Dr. Tilman Pfau, for the possibility to write my bachelor's thesis at the 5th Institute of Physics.
- Dr. Tim Langen, for awakening my interest in atomic physics with his interesting lecture and for giving me the possibility to write my bachelor's thesis in the Cold Molecules team.
- Phillip und Ole, for explaining the experimental setup to me, answering all my questions, proofreading of my thesis and general great support.
- All other members of the institute, for having lunch breaks together, letting me borrow equipment and for their support with technical problems.
- My family, friends and fellow students for their support and motivation during my studies.